SEISMICITY AND STRESSES IN THE KANTISHNA SEISMIC CLUSTER, CENTRAL ALASKA

A
THESIS

Presented to the Faculty

of the University of Alaska Fairbanks

in Partial Fulfillment of the Requirements
for the Degree of

MASTER OF SCIENCE

By

Lea A. Burris

Fairbanks, Alaska

December 2007

Abstract

The Kantishna Cluster is an enigmatic and energetic cluster of earthquakes located in central Alaska, just to the northwest of Mt. McKinley/Denali and adjacent to the Denali Fault. The Kantishna Cluster has no visible fault traces, and is often speculated to have a connection to the Denali Fault. The Kantishna Cluster is located at a hub of tectonic activity including Bering Block rotation to the west, bookshelf faulting to the northeast, and rotation of southern Alaska due to Pacific plate convergence to the south.

The intention of this study was to broaden the knowledge base about the Kantishna Cluster and use the M_w 7.9 Denali Fault earthquake to find a relationship between the cluster and the Denali Fault Zone. Rate calculations in conjunction with z- and b-value changes show that the Denali Fault earthquake had little influence on the seismicity of the Kantishna Cluster, with the exception being the southern most portion closest to the Denali Fault. The highly variable background rate of seismicity in the Kantishna Cluster makes seeing changes in the seismicity difficult. Stress tensor inversions suggest a change in the stresses in the Kantishna Cluster; however, triangle diagram comparisons show that the pattern of earthquake mechanism types did not change. Coulomb stress change calculations predict small changes that were not observed in the data. Double difference hypocentral relocations show that the cloud of earthquakes collapses down to several distinct features.

Seismicity trends resolved from hypocentral relocations made it possible to infer fault planes or planar structures in the region. The newly uncovered structures are utilized in the formation of a model involving two wedges to describe the seismicity in the Kantishna Cluster. The two wedges are being “squeezed” in opposite directions accommodating for compression across the cluster due to Pacific plate convergence.

Table of Contents

List of Figures

Page

List of Tables

Page

Acknowledgements and Dedication

I would like to thank my friends and family for all of their support throughout my academic career. I would like to thank my fiancé Matthew Gardine for his unwavering support, and his help with programming and proofreading. I would like to thank my undergraduate professors, Kurt Friehauf, Sarah Tindall, Ed Simpson, and Paul Quinn, for guiding me through undergrad, encouraging me to go farther and for always being willing to help with any questions I still have. I'd like to thank my UAF professors, Jeff Freymueller and Steve McNutt, for their help with even the simplest questions. Last but certainly not least, I'd like to thank my committee, Doug Christensen, Natasha Ruppert, and Mike West, for both their group and individual efforts in driving me to succeed. I would like to thank my advisor, Roger Hansen, for giving me the opportunity to spend a few years in Alaska doing something I have dreamed about since I was seven years old...studying earthquakes.

I'd like to dedicate this thesis to several people. First to my two grandfathers, Robert Robenolt and Russell Burris, who passed away and were not able to see me accomplish this goal. I know they would be very proud of me. Secondly, to my parents for instilling in me a sense of value in education. Thirdly, I wanted to dedicate this work to the people who have reinforced in me a drive to succeed despite any obstacle. Without their support or criticism, my life would have turned out very differently.

Chapter 1. Introduction and Background

The Kantishna Seismic Cluster is the most seismically active crustal source region in interior Alaska; with 200+ locatable earthquakes yearly confined to a 65km by 70km area. The Kantishna Cluster is located northwest of and adjacent to Mt. McKinley (Denali, the highest point in North America) and just north of the Denali Fault Zone (see Figure 1.1). The Kantishna Cluster is nestled in the foothills of the Alaska Range. The northern most portion of the Kantishna Cluster is the area known as the Kantishna Hills. The Kantishna Hills area is characterized by a northeast-trending anticlinorium; cored by mica schist and framed by deformed tertiary strata (Lesh and Ridgway, 2007).

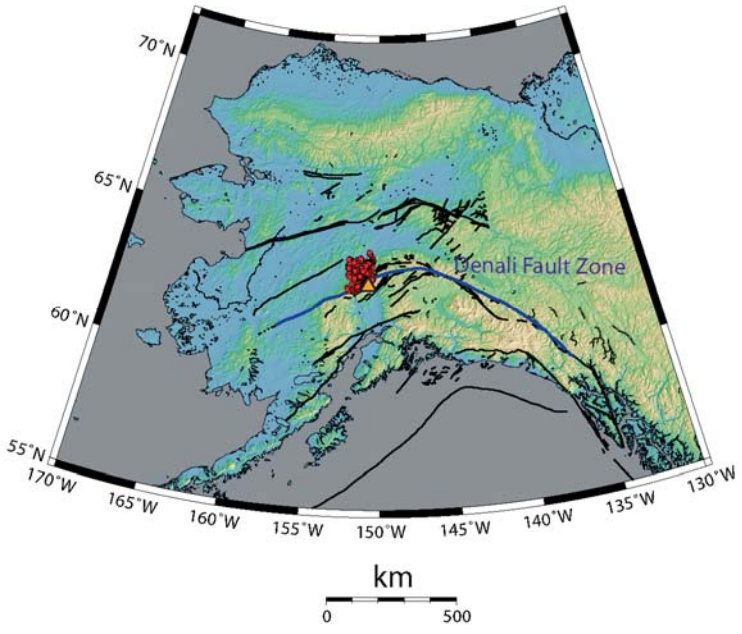

Figure 1.1 Location of Kantishna Cluster in Central Alaska. The red dots represent earthquakes in the Kantishna Cluster. The blue line is the Denali Fault and the orange triangle represents Mt. McKinley/Denali. The black lines are additional faults in Alaska.

The basement rocks in the Kantishna Hills area are regionally metamorphosed, ranging in age from Precambrian to late Paleozoic (Bundtzen, 1981). The most extensive rock unit is the Birch Creek Schist. The Birch Creek Schist consists of a shallow-water continental-shelf sequence that was metamorphosed into quartzite, quartz-mica schist, feldspar-biotite schist, gneiss, marble and greenstone (Bundtzen, 1981). Three additional rock units comprise the Kantishna Hills area, the Spruce Creek sequence, the Keevy Peak Formation and the Totatlanika Schist. These three units are metamorphosed volcanic and sedimentary rocks that interfinger locally and are believed to represent an early Paleozoic rift environment formed on the Birch Creek shelf deposits (Bundtzen, 1981; Eppinger et al., 2000). The Kantishna region has been uplifted with the Alaska Range since the middle Tertiary and isoclinal to open folds and faults are common to the area (Eppinger et al., 2000). Miocene sandstone and shale and Quaternary gravel overlie the older rock (Bundtzen, 1981). Lesh and Ridgway (2007) used stream profiles and erosional features to show that the Kantishna Hills area is an actively deforming and currently uplifting environment.

The Kantishna Cluster lies at the southwest extension of the Minto Flats seismic zone. The Minto Flats seismic zone is one of a series of left-lateral strike-slip fault zones, which includes the Fairbanks and Salcha seismic zones, which outline clockwise rotating blocks between the right-lateral motions of the Denali Fault to the south and the Tintina fault to the north (Page et al., 1991, 1995) (see Figure 1.2). The rotation of these blocks accommodates shortening in central Alaska due to north-northwest compression resulting from Pacific plate convergence. South of the Denali Fault, counter-clockwise rotation of

southern Alaska due to the collision of the Yakutat block, and in western Alaska, clockwise Bering Block rotation contribute to the regional stresses (Figure 1.3) (Eberhardt-Phillips et al., 2003; Cross and Freymueller, in press).

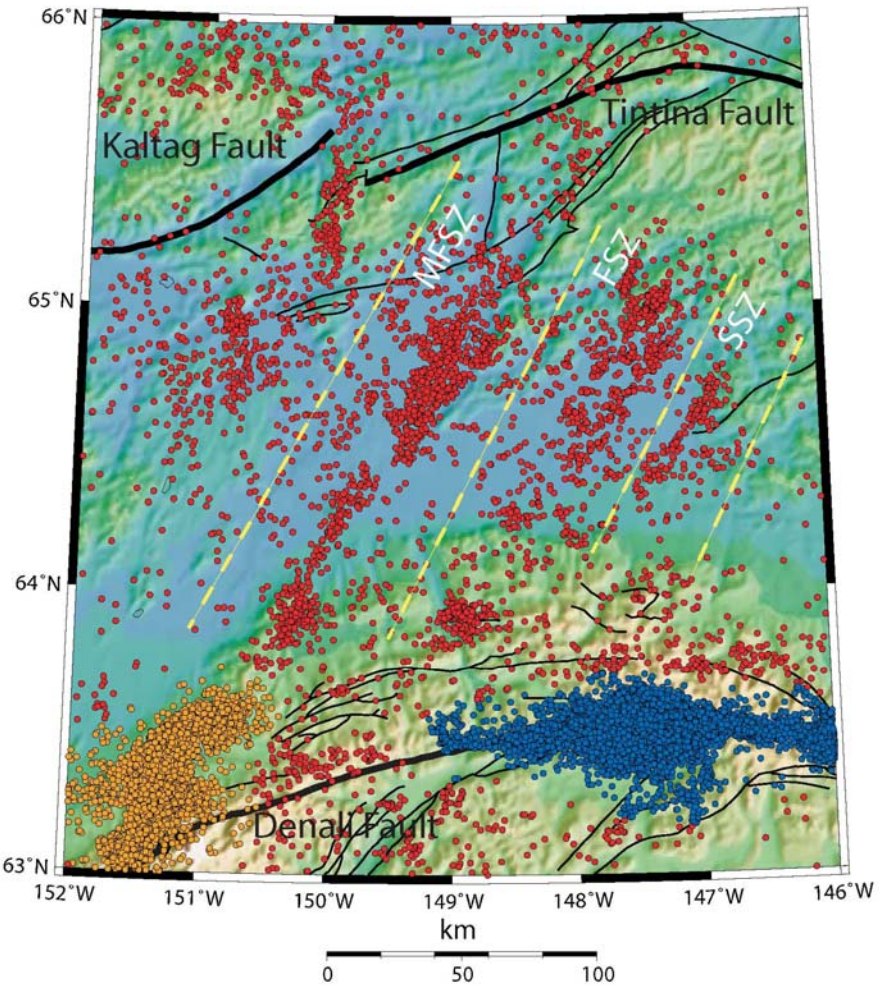

Figure 1.2 Map of Central Alaska Seismicity. This map shows the seismicity of central Alaska from 1970 to 2006.25. The blue dots represent aftershocks of the M_w 6.7 Nenana Mountain foreshock and the M_w 7.9 Denali Fault earthquake. The orange dots represent the Kantishna Cluster. The yellow dashed lines outline the three left-lateral strike-slip fault zones, labled Minto Flats Seismic Zone (MFSZ), Fairbanks Seismic Zone (FSZ) and Salcha Seismic Zone (SSZ). The thick black lines show the Kaltag and Tintina Faults to the north and the Denali Fault to the south.

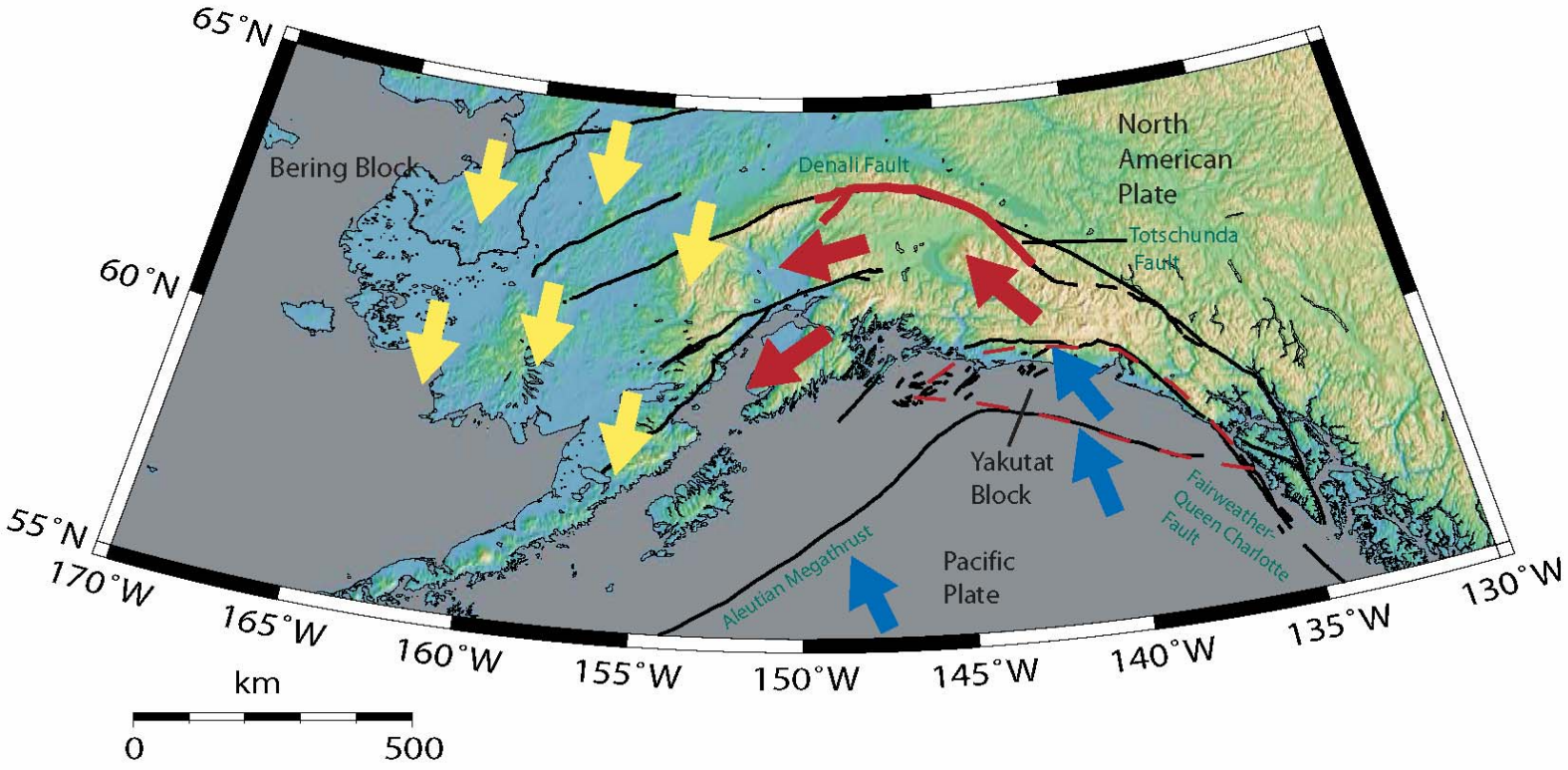

Figure 1.3 Central Alaska Tectonics. This figure shows the tectonics in central Alaska. The blue arrows show plate motions of the Pacific Plate and the Yakutat Block with respect to Alaska. The red arrows show the approximate rotation of southern Alaska. The yellow arrows show the predicted motion of the Bering plate. The red dashed line estimates the outline of the Yakutat Block. The bold red line shows the rupture of the M_w 7.9 event on 3 November, 2002 and the M_w 6.7 Nenana Mountain foreshock. Modified from Eberhart-Phillips et al., 2003; Cross and Freymueller, in press.

Within the cluster, dozens of small earthquakes occur daily, with a local magnitude (M_L) 2 or greater every other day and at least one $M_L \geq 4$ each year. The total cumulative moment from 1990 through 2006.25 amounts to the equivalent of one moment magnitude (M_w) 5.46 earthquake. Figure 1.4 shows the total cumulative moment with events $M_L \geq 4$ plotted as vertical lines. The earthquakes are generally shallow with depths less than 25km (see Figure 1.5). There are a few anomalous events down to depths of about 60km. These events are enigmatic because the estimated crustal thickness in the region is roughly 50km (Meyers et al., 2000; Veenstra et al., 2006) and the subducting slab reaches depths below 140km (see Figure 1.6). Ratchkovski and Hansen (2002) found that joint hypocentral determination relocations break the cluster into two trends of seismicity aligned roughly SW-NE and WNW-ESE and that the stresses change rapidly across the region. However, the origins of the seismicity in the region are still unknown.

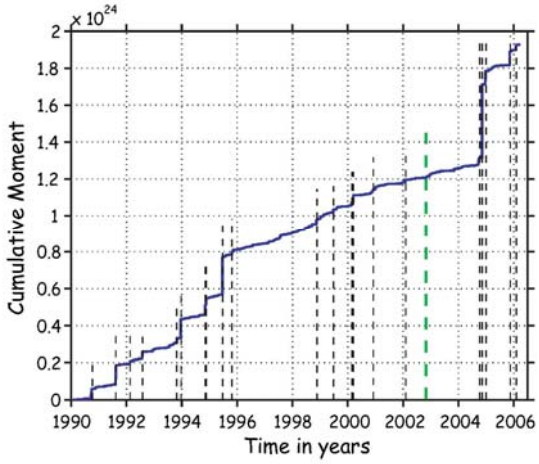

Figure 1.4 Cumulative Moment Plot. Above is the plot of cumulative moment release for the entire Kantishna Cluster from 1990-2006.25. The vertical lines represent events of $M_L \geq 4$ in the cluster. The green line in 2002 denotes the occurrence of the M_w7.9 Denali Fault earthquake.

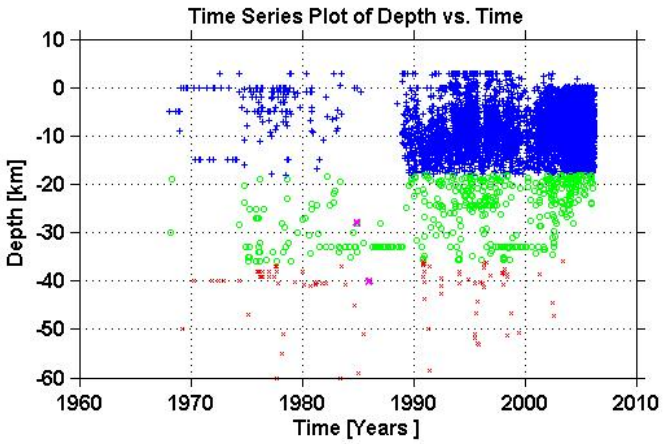

Figure 1.5 Depth Time Series Plot. This plot shows the depths of earthquakes in the Kantishna Cluster. Note the gaps in data prior to 1990 and the anomalous "deep" events plotted down to 60km. The colors and symbols represent different depth intervals: blue (+) represents 0-17.6km, green (o) represents 17.6-35.2km, and red (x) represents 35.2-60km.

The Denali Fault stands out as the major fault system in the region. The Denali Fault is an intracontinental right lateral strike-slip fault that accommodates a portion of the oblique collision of the Yakutat block into the southern Alaska margin (Eberhart-Phillips et al., 2003) (see Figure 1.3). Historically, there has been little activity on the Denali Fault, especially the western portion (see Figure 1.6). However, on 3 November 2002, a M_w 7.9 earthquake ruptured the central Denali Fault. The rupture began on the Susitna Glacier Fault then propagated east along the Denali Fault and terminated on the Totschunda Fault (Eberhart-Phillips et al., 2003). The Kantishna Cluster is located roughly 150-200km WNW of the nucleation point of the M_w 7.9 event. The juxtaposition of the Kantishna Cluster and the seismically inactive western portion of the Denali Fault lead many to speculate on a connection between the two. The M_w 7.9 event lends an

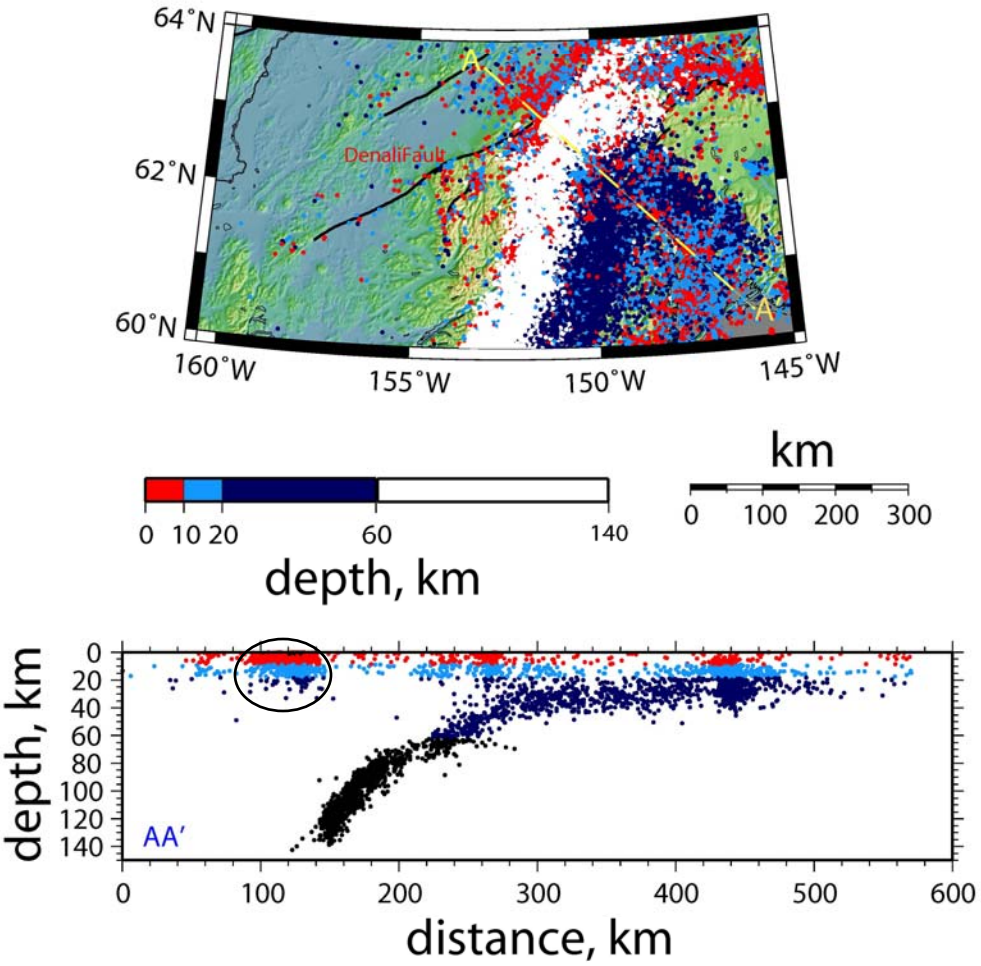

Figure 1.6 Map of Southern Alaska with Cross Section. The map above shows the seismicity of southern Alaska and the western Denali Fault. All earthquakes since 1990 are plotted with color assigned based on depth. The 10km wide cross section (from A to A') shows the subducting slab. Events below 60km depth are plotted black in the cross section for visibility. The cluster of shallow earthquakes around 100-120km (circled) in the cross section is the Kantishna Cluster.

opportunity to monitor changes in seismicity and stresses in the Kantishna Cluster preceding and following the M_w 7.9 event to determine the impact on the region.

The emphasis of this study was to acquire more knowledge about the Kantishna Cluster, and determine what effect, if any, the M_w 7.9 Denali Fault earthquake had on the seismicity in the cluster. From these changes, it may be possible to determine some kinematic or dynamic relationship between the two, and provide more insight into the origin of the cluster and the role it plays in the seismicity of interior Alaska. Double difference hypocentral relocations were used in conjunction with spatial and temporal analysis of both b- and z-values to determine any changes potentially related to the M_w 7.9 event. Double difference hypocentral relocations were also used to infer fault planes that give a first glimpse of the geometry of the Kantishna Cluster. Stress tensor inversions for events greater than M_L 3 were used to determine the stresses in the cluster before and after the M_w 7.9 event. Predicted Coulomb stress changes were calculated to show the degree of change on each of the planar structures found.

Chapter 2. Data

The first step in the analysis of the Kantishna Cluster is to define the region that represents the entire cluster. I started with a broad search of the Alaska Earthquake Information Center (AEIC) earthquake catalog using a rectangular area with latitudes between 62.5°N and 64°N and longitudes between 152.5°W and 150.5°W. The vast majority of the earthquakes fall within 62.9°N to 63.7°N and 151.75°W to 150.5°W. Since this is a crustal study, I chose a maximum depth of 60km to include the anomalous "deep" events but exclude those of the subducting slab. This resulted in 8,174 events with magnitudes between 0.2 and 6.9 (in 1932). Ratchkovski (2001) showed that the stresses change rapidly across the cluster. To address this in more detail, I've divided the cluster into three subsections: north (63.33°N-63.65°N, 151.75°W-150.5°W), central (63.23°N-63.33°N, 151.75°W-150.8°W), and southern (62.9°N-63.23°N, 151.75°W-151.1°W), labeled 1, 2, and 3 respectively (see Figure 2.1). Figure 2.1 shows the seismicity in the Kantishna Cluster with event symbol size based on magnitude and colored by depth.

Currently, the AEIC has several broadband seismic stations in the vicinity of the Kantishna Cluster. Prior to the M_w 7.9 Denali Fault earthquake there were two broadband stations operational, Kantishna Hills and Thorofare Mountain. After the Denali Fault earthquake three more broadband stations were installed, Purkeypile, Bear Paw Mountain and Lake Michumina (see Figure 2.1). Table 2.1 shows the on-dates and locations of the broadband stations near the Kantishna Cluster.

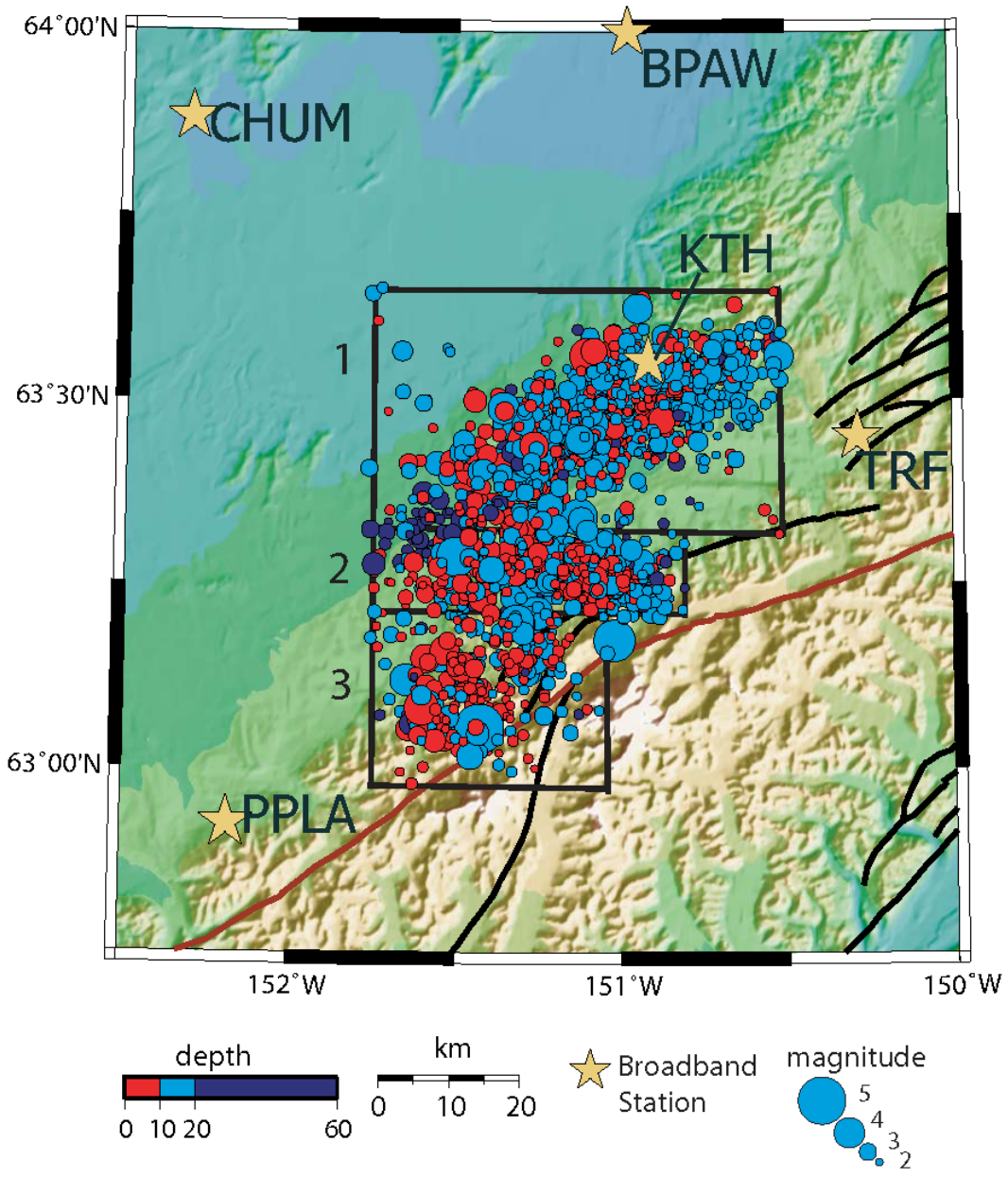

Figure 2.1 Map of Subsections. This map shows all earthquakes $M_L \geq 2$ since 1990. The black boxes outline the three subsections numbered 1, 2, and 3, from north to south. Circles are sized based on magnitude and colored by depth. The dark red line represents the Denali Fault with the other nearby faults plotted in black. The broadband stations closest to the Kantishna Cluster are plotted as yellow stars.

Table 2.1. Broadband Stations in the Vicinity of the Kantishna Cluster Showing Their Locations and On-dates.

Station name	Kantishna Hills (KTH)	Thorofare Mt. (TRF)	Purkeypile (PPLA)	Bear Paw Mt. (BPAW)	Lake Michumina (CHUM)
Location	63.5532N 150.9209W	63.4510N 150.2872W	62.8968N 152.1870W	64.1002N 150.9848W	63.8827N 152.3147W
On-date	2003.44	2003.43	2002.94	2004.38	2004.42

Since the station coverage in the Kantishna Cluster has changed during the time period studied here, the magnitude of completeness (Mc) has changed. A Mc for the whole dataset is required for an accurate comparison of older and newer data. The Mc, or detection threshold of a catalog is the value at which all events with a larger magnitude should always be detected. At the time of this study, the large number of aftershocks following the M_w7.9 Denali Fault earthquake caused a backlog in data processing so that essentially only events larger than M_L 2 were located. To obtain the Mc, I used the maximum curvature of the frequency-magnitude distribution. The frequency-magnitude distribution plots cumulative number of events versus magnitude. The power-law relationship of earthquake frequency and magnitude says this line should be linear (Lay and Wallace, 1995). In reality, this line is not straight. The point of maximum curvature of the plot is the magnitude of completeness for the catalog. The Mc for the entire catalog is 1.7. A plot of the magnitude of completeness with time shows that the Mc changes significantly temporally, as low as 0.5 in 2004, most likely related to monitoring upgrades (see Figure 2.2). To insure consistency, I chose a Mc of 2.0. There are 2,906 events with $M_L \geq 2$.

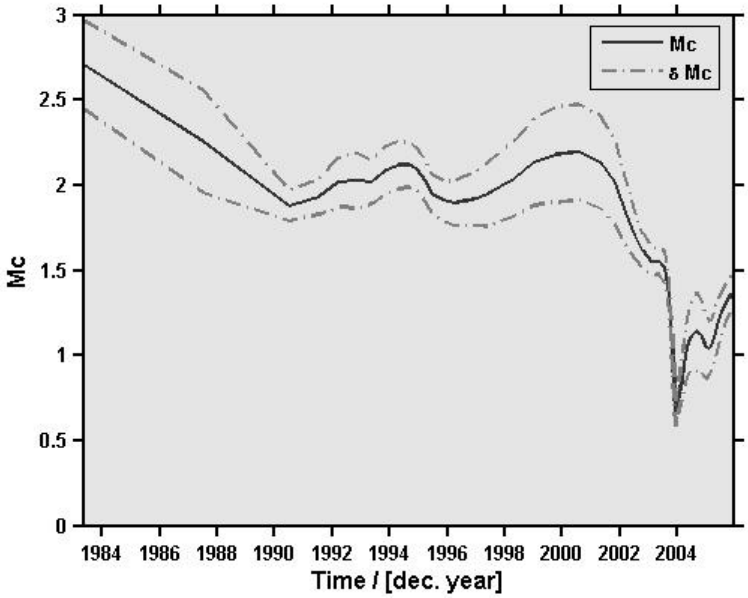

Figure 2.2 Plot of Magnitude of Completeness with Time. The Mc hovers around 2 after 1990 except for the steep drop off in 2003. The uncertainties associated with the Mc change throughout time as well, increasing in 1996 and then dramatically improving in 2001.

In addition to instrument upgrades, software changes have occurred. In 1988 a digital recording and processing system was introduced, which significantly improved data quality, revealing gaps in the data set prior to 1988. Therefore, in this study, only data from 1990 and beyond were used for the purposes of rate calculations (2,163 events). In 1996, the AEIC changed part of the programming scheme for the automatic event triggers and dbloc2 was introduced for data processing. Due to this change, the uncertainties in Figure 2.2 increase from 1996 to 2001, possibly due to missed events. In 2001, AEIC analysts began manually scanning the waveforms to pick arrivals. Manual scanning for events and the addition of new stations caused the uncertainties to decrease, as well as the Mc.

The sparse station coverage at the beginning of the catalog and the automatic locations generated result in a cloud of earthquakes with no discernable orientations or structures. Hypocenter relocations were used to improve earthquake hypocenters and help resolve earthquake trends.

Chapter 3. Double Difference Hypocentral Relocations

3.1 HypoDD

Hypocentral relocations were used to determine the relative locations of all earthquakes in the Kantishna Cluster. Improved locations better define the cluster and allow for a better spatial analysis throughout the cluster. From AEIC catalog locations, the cluster appears as an S-shaped cloud with three parts. Ratchkovski (2001) relocated a set of earthquakes in the Kantishna Cluster, showing the cloud of earthquakes collapsing down to two distinct strands of seismicity. Subsection 3 is visible in the results from Ratchkovski (2001); however, the smaller cluster is more prevalent in the recent database and was included in this study.

To do the double difference relocations, I used HypoDD. HypoDD is a program package for relocating earthquakes with the double difference algorithm of Waldhauser and Ellsworth (2000). If the hypocentral separation between two earthquakes is small compared to the distance between the event and the station recording it, then the ray paths between the source region and a common station are similar along nearly the entire ray path. Therefore, the difference in travel time observed at the common station can be attributed to the spatial offset between the two events (Waldhauser and Ellsworth, 2000). The technique of Waldhauser and Ellsworth (2000) allows the simultaneous relocation of large numbers of earthquakes over large distances. The algorithm combines P- and S-wave differential travel times with travel time differences formed from catalog data and minimize residual differences (or double differences) for pairs of earthquakes by

adjusting the vector difference between the hypocenters. Essentially the algorithm shifts the hypocenters to better fit the travel time differences between the two events.

The double difference algorithm calculates travel times in a layered velocity model (where velocity depends only on depth) for the current hypocenters (Waldhauser, 2001). The double difference residuals for pairs of earthquakes at each station are minimized by weighted least squares using the conjugate gradients method (LSQR) (Paige and Saunders, 1982). The solutions are found by iteratively adjusting the vector differences between hypocentral pairs, with the locations and partial derivatives being updated each time (Waldhauser, 2001). Events in the Kantishna Cluster were relocated two ways. First, all events were relocated using all stations common to the events. Second, events that are more recent were relocated using information from the more recently installed broadband stations. Figure 3.1 shows the distribution of stations within roughly 200 km of the center of the cluster. All stations operational at some point during the study interval, including temporary stations, are plotted. The color scheme represents the duration of operation during the study period.

3.2 Relocations for All Events $M_L \geq 2$

All events from the AEIC catalog fitting the criteria discussed in chapter 2 were relocated. The dataset included all events $M_L \geq 2$ within the criteria discussed in chapter 2 (2163 events). Stations up to 400 km were used in the relocation, to include more phases in the relocation due to the sparse station coverage at the beginning of the data set. Each hypocenter was relocated with surrounding hypocenters located within a radius of 10 km.

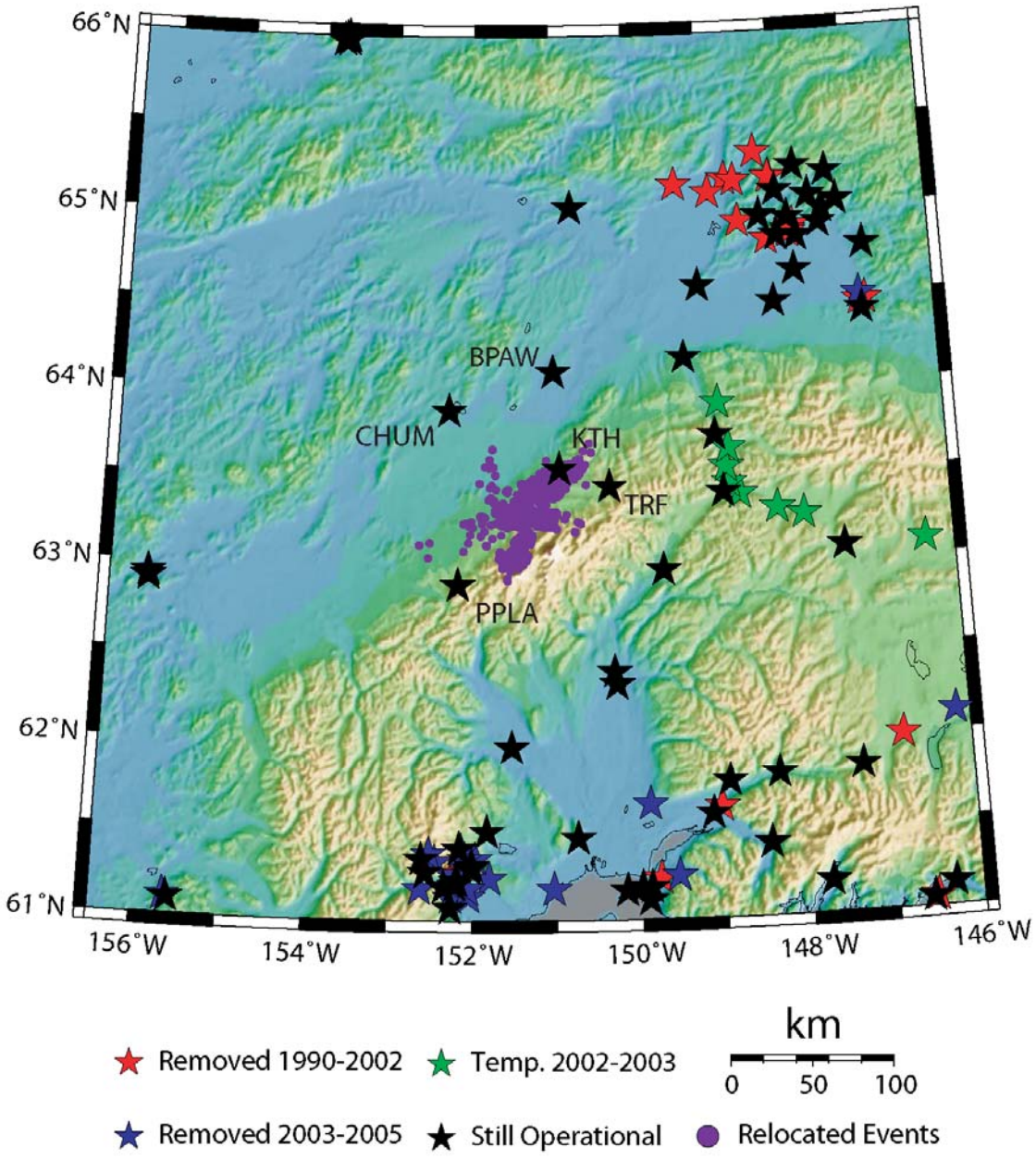

Figure 3.1 Map of Station Coverage Used in the Relocations. All stations operational or added since 1990 are plotted, including temporary stations. The colors coincide with the removal dates of the instruments. The labeled stations are the broadband stations closest to the Kantishna Cluster.

The velocity model used in the relocation is the northern Alaska velocity model used by the AEIC in routine processing with a V_p/V_s ratio of 1.76 (Table 3.1).

Table 3.1 Velocity Model Used in the Relocations

Layer Depth (km)	0 - 24.4	24.4 – 40.2	40.2 - 76	76+
Velocity, V_p (km/s)	5.9	7.4	7.9	8.29

Of the 2163 events used in the relocations, 2118 events relocated successfully. Events deemed successfully relocated fit the criteria of having at least 8 common arrivals between event pairs whose origins are within 10km of each other. The limbed cloud of earthquakes collapsed down into three, possibly up to six, separate features. Figure 3.2 shows the relocation results. The plots in Figure 3.3 show the amount of change in hypocenter locations (latitude, longitude, and depth) plotted against their original locations. The change in latitude shows that the majority of the hypocenters moved to the north with an average shift of 0.02° (approx. 2.23km) and the hypocentral longitudes shifted west 0.075° (approx. 3.80km). Since the relocations are relative to the events, not a fixed location, the relocations resulted in an overall cluster translation to the north-west. However, not all hypocenters moved to the north and west, showing that although the overall shift was north-west, the hypocenters did collapse into a tighter cluster (see Figures 3.2 and 3.3). The depth changes plotted in Figure 3.3, show that shallower events relocated deeper and deeper events relocated shallower by an average of 3.5km, implying an overall tightening of the hypocentral depths.

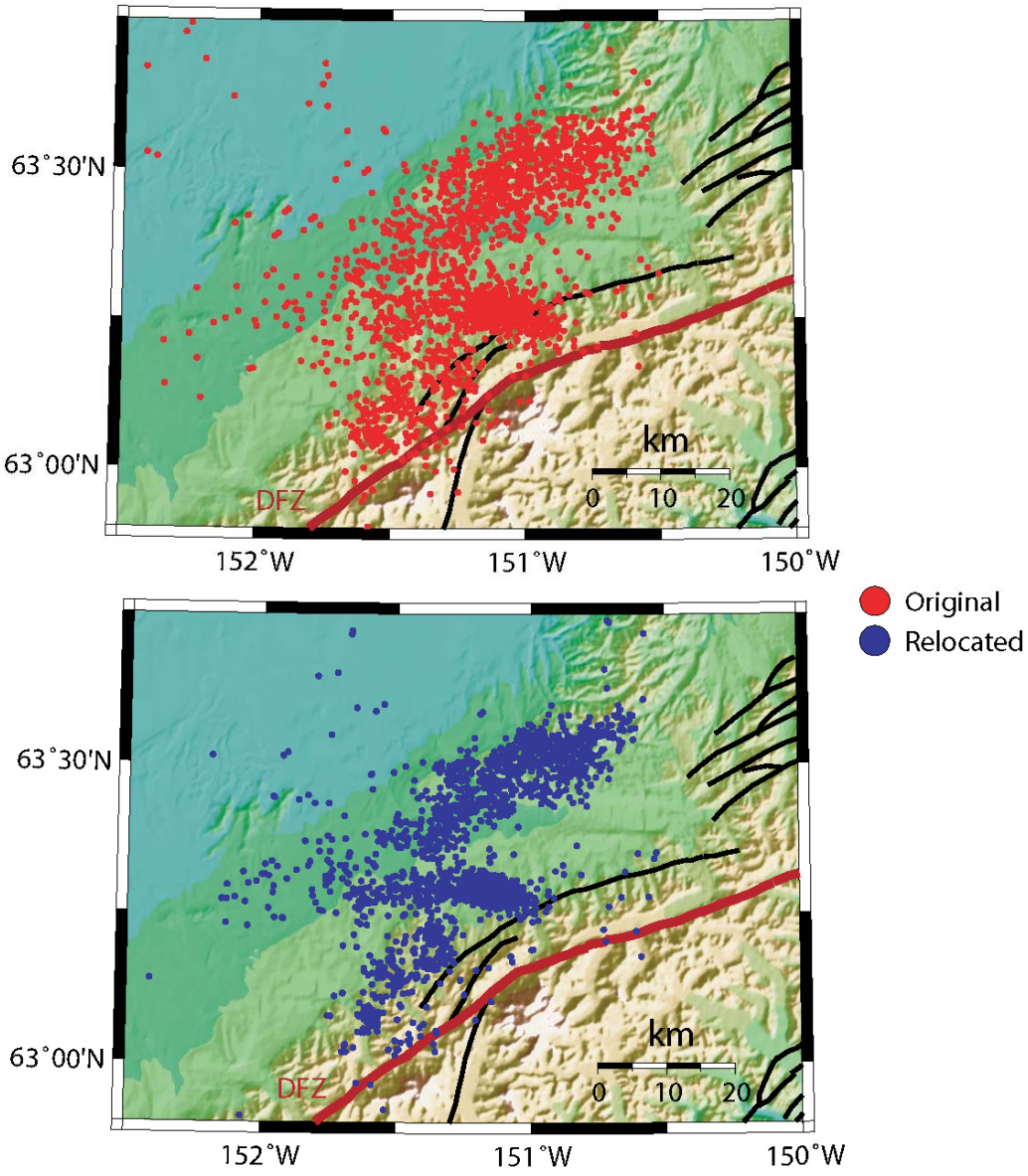

Figure 3.2 Relocation Results for All Data After 1990. The original events are plotted in red and the relocated events plotted in blue. The dark red line represents the Denali Fault. The relocated events collapse the cluster down into three definite and possibly six features.

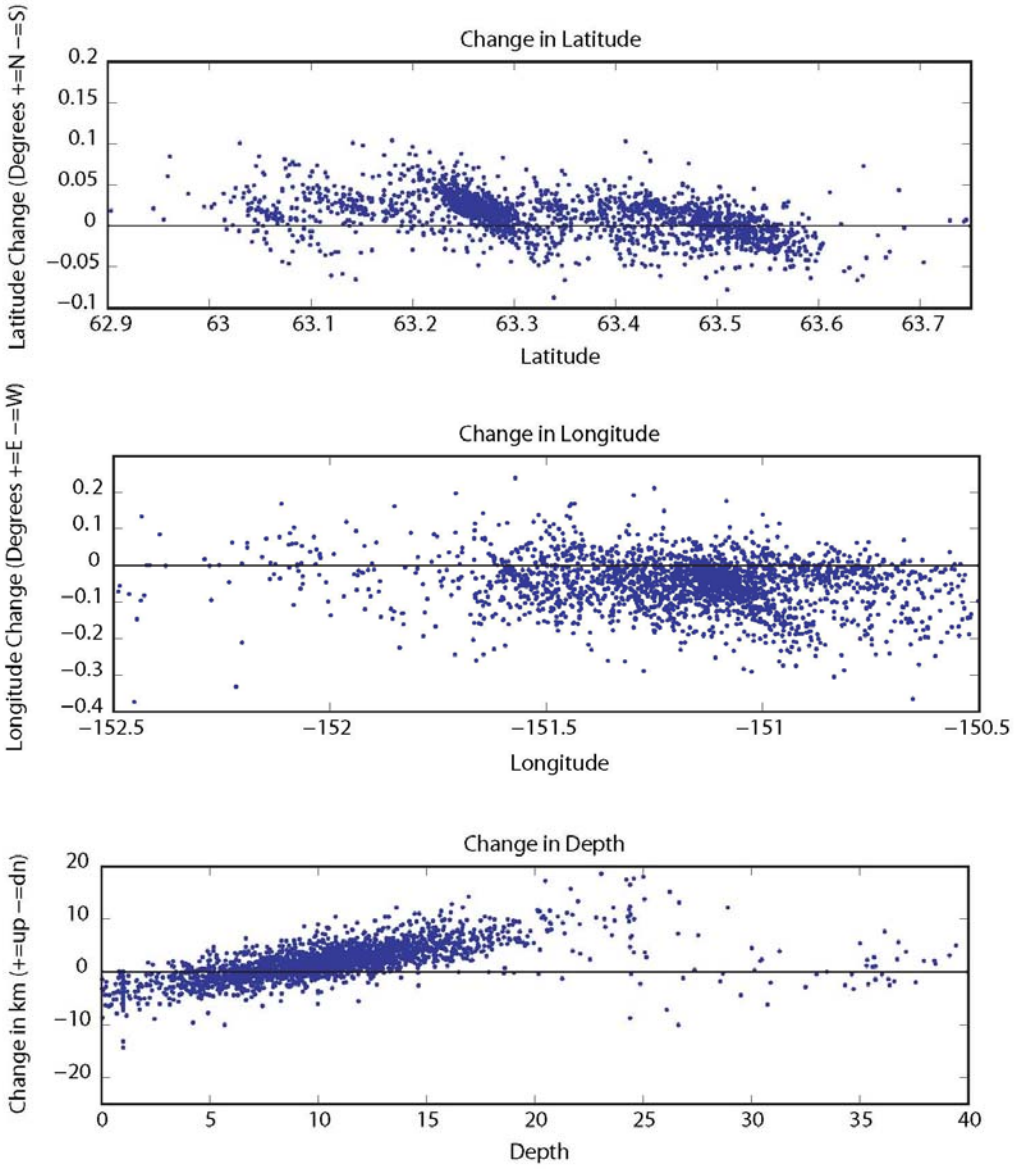

Figure 3.3 Plots of Amount of Hypocenter Change During the Relocation. The plots show the amount of change in latitude, longitude, and depth, respectively, plotted against their original location. The top figure shows events overall moved northward with several events moving southward showing a collapse of the cluster in a north-south direction. The middle figure shows events moved westward with several events having moved eastward showing an overall collapse in an east-west direction. The bottom figure shows shallower depths, above 5km, shifting deeper and deeper events, deeper than 10km, shifting shallower. The depth changes suggest that not only did the cluster collapse in map view but also in depth.

Figures 3.4-3.6 show the relocation results with appropriate cross sections. Looking at subsection 1 (Figure 3.4), the cluster appears to bend at 63.4°N-151.3W implying the possibility of a separate structure. A cross section along the subsection, at a strike of 76° (AA') bisected by a line striking 166° (AxAx'), shows a planar feature dipping roughly 50° to the south resolved as a result of the relocations (black dashed line in cross section AxAx'). The depths condensed considerably to show the dipping plane. A cross section along subsection 2 (Figure 3.5) striking 89° bisected by a line striking 179°, shows the depths collapsing significantly to reveal a vertically dipping planar feature (black dashed line in cross section CxCx') at the eastern end of the cluster, potentially two separate structures. The dashed box outlines the planar feature whose cross section is shown in CxCx'. A cross section through subsection 3 (Figure 3.6) striking 59° shows the subsections to be defined by two separate features. Cross sections striking 149° through each of the two features shows the clusters collapsing to form two distinct features. The southern portion resembles a vertically dipping feature whereas the northern portion resembles 149° striking feature that dips to the north. The dashed boxes outline the inferred planes and the dashed lines show the inferred dip of the planes.

The relocations showed a significant improvement in the hypocentral locations. Various structures were resolved through not only latitude and longitude changes but also through depth resolution. Apparent dips in the planar structures are evident as a result of the relocations.

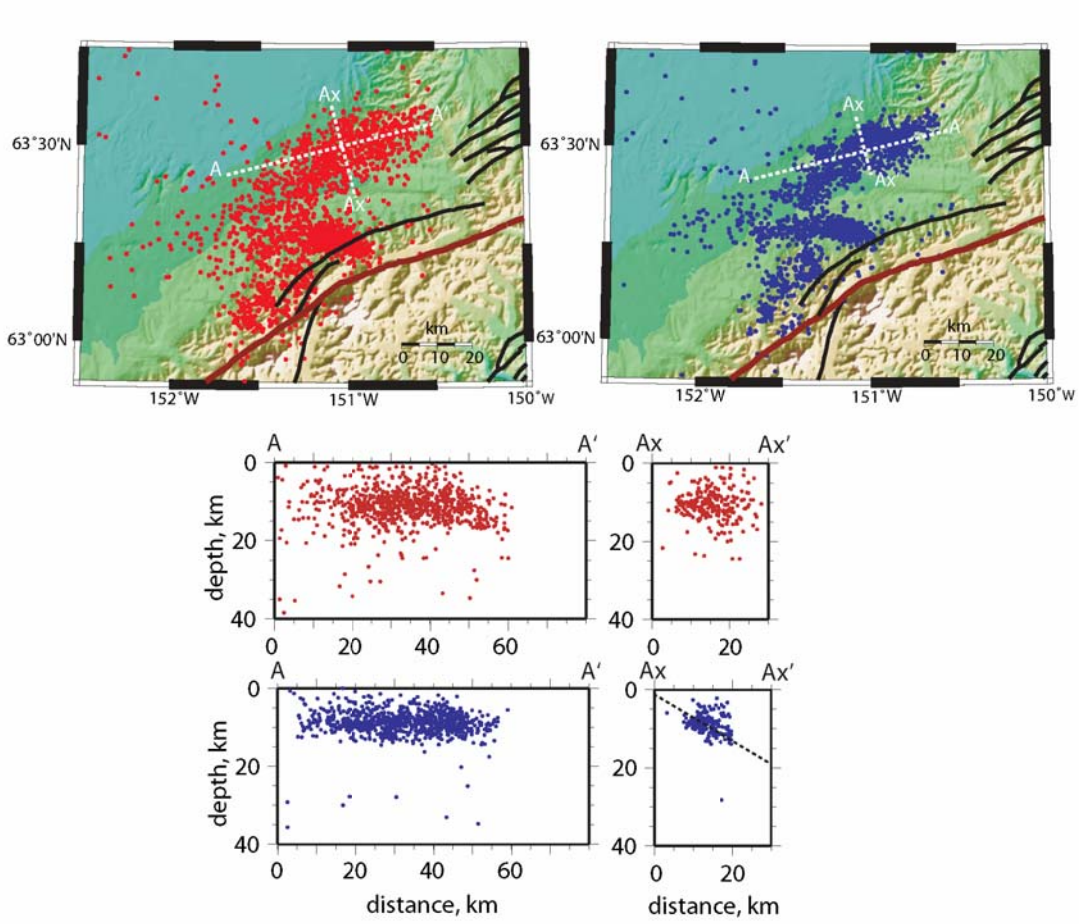

Figure 3.4 Relocation Result Cross Section for Subsection 1. The red dots represent the original hypocenters and the blue are the relocation results. AA' strikes 76° and shows the depths collapsing to revealing a planar structure roughly 10km thick. The bisecting line AxAx', striking 166° shows that the depths collapse to show the plane dips roughly 50° (black dashed line) from horizontal.

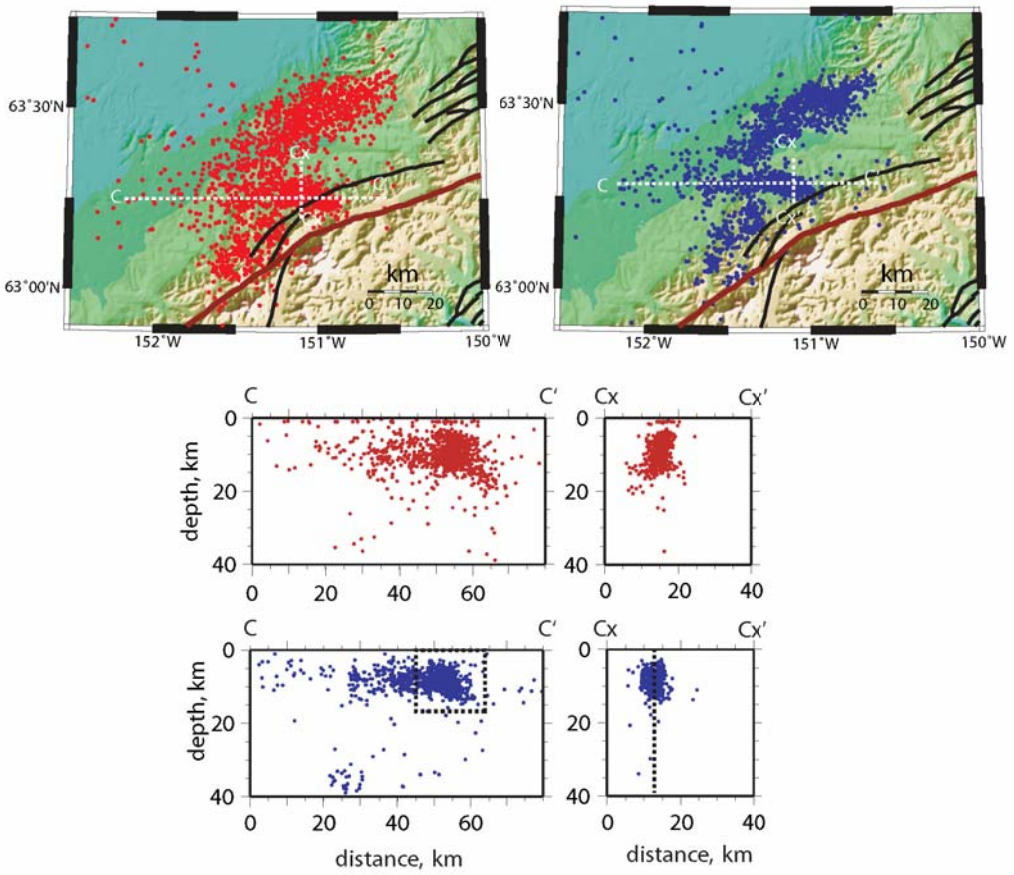

Figure 3.5 Relocation Result Cross Section for Subsection 2. The red dots represent the original hypocentral locations and the blue the relocated hypocentral locations. The cross section CC', striking 89°, shows the depths collapse considerably to reveal a planar structure 10 km thick. A bisecting cross section, CxCx', of the eastern portion of subsection 2 (black dashed box) shows the planar feature (black dashed line) is vertically dipping.

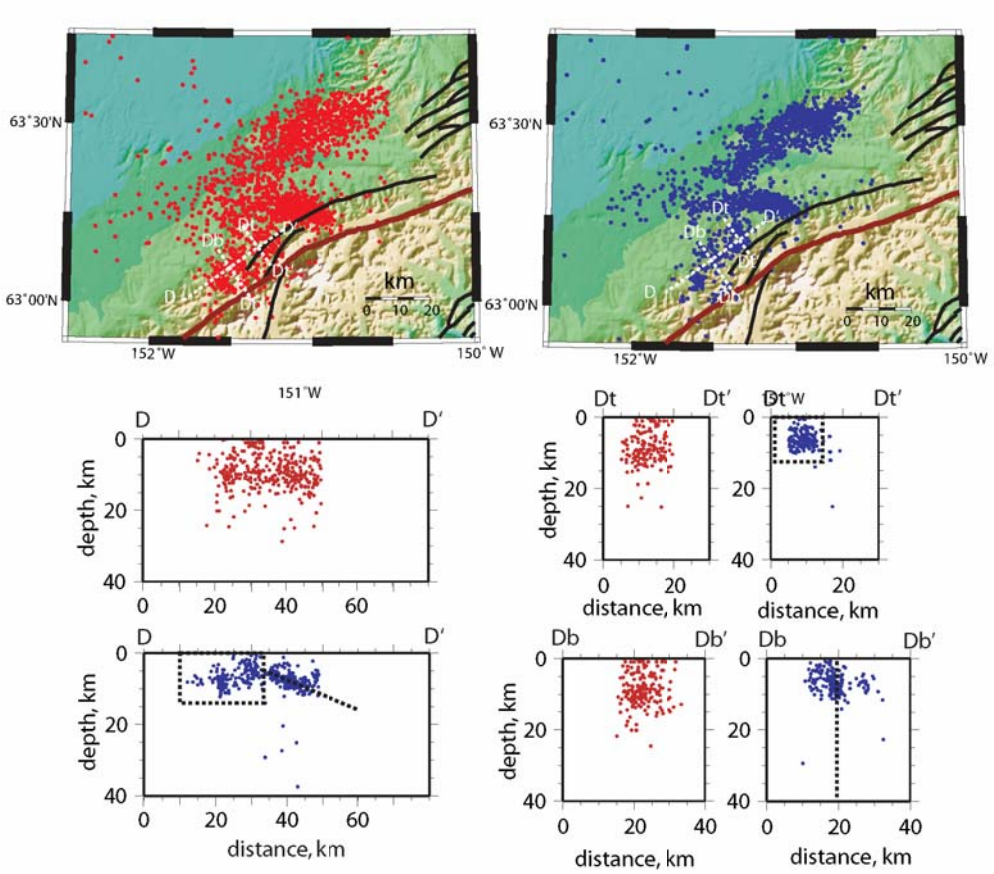

Figure 3.6 Relocation Result Cross Section for Subsection 3. The original hypocentral locations are plotted in red and the relocated hypocenters are plotted in blue. A cross section striking 59°, DD', shows the depths collapsing to reveal 2 different structures. The structure to the north-east appears to dip to the north-east roughly 60° (black dashed line in DD') from horizontal. The structure to the south-east is either planar or vertically dipping (black dashed box in DD'). Two bisecting cross sections are shown; DtDt' to the north and DbDb' to the south. DtDt' shows the depths collapsing to reveal a 10km thick planar feature (black dashes box). DbDb' shows the depths collapsing to show a vertically dipping feature (black dashed line).

3.3 Relocations of Events with Newer Stations

The addition of several broadband stations in and around the Kantishna Cluster improved the analysts' ability to locate earthquakes in the cluster. Since HypoDD uses arrivals at common stations for all events, looking at recent events which contain the new broadband stations show a significant improvement in defining the structure of the Kantishna Cluster. Since the relocation is calculated using stations common to events in the proximity of the events, the newer broadband station data may not have been used in the overall relocation with the older events. Here the more recent events were relocated using the newer data; the same parameters from section 3.2 were used, however only stations within 200 km of the cluster center were used. All earthquakes falling in the cluster after 2004.42 (the date of the most recent broadband installation, see table 1) regardless of magnitude were used, for a total of 2096 events with magnitudes ranging from 0.1 to 5.

Figure 3.7 shows the relocation results. A total of 1861 events were successfully relocated. As in section 3.2, the trends collapse significantly. Each subsection appears to break down into two smaller regions that are more discernable. Figure 3.8 shows the amount of hypocentral change in latitude, longitude and depth. The amount of change is plotted against its original value. Overall, the hypocentral latitudes shifted southward with an average of 0.016° (1.78km). The hypocentral longitudes shifted eastward with an average of 0.031° (1.57km). These hypocentral translations are opposite in sense of direction from those of the whole data set (section 3.2). The depths, however, followed the same trend as in section 3.2. The deeper events became shallower and the shallow

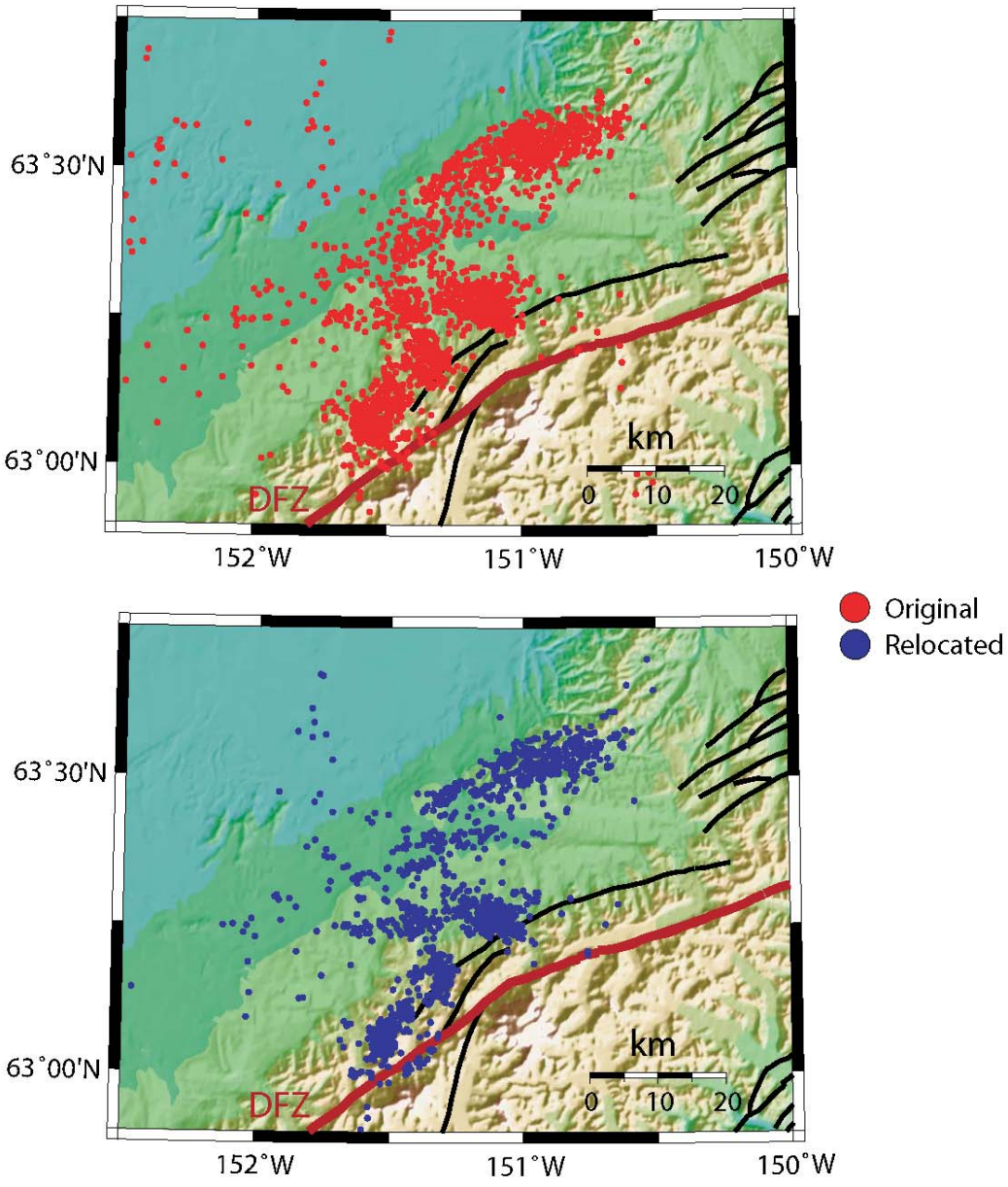

Figure 3.7 Relocation Results for Earthquakes After 2004. All events in the catalog regardless of magnitude were relocated and are shown here. The original hypocenters are colored red and the relocated hypocenters are blue. The relocation results show the amount of scatter significantly decreased and the clusters collapsed onto themselves to better define the structures present. The smaller segments of each subsection become more visible.

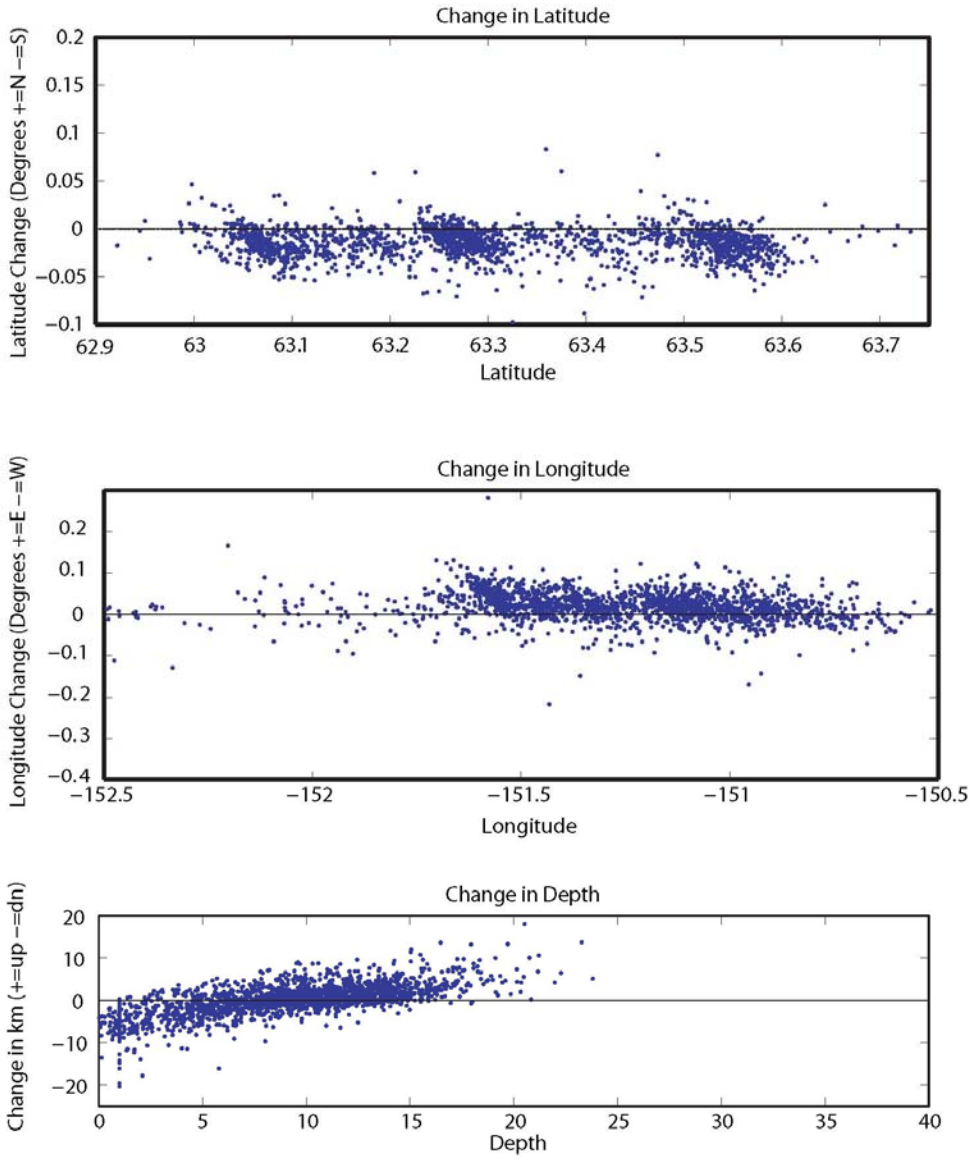

Figure 3.8 Plots of Hypocentral Change Resulting from the Post-2004 Relocations. Changes in hypocentral latitude, longitude and depth, respectively, are plotted versus their original value. Latitude changes trend southward while several events shifted northward, showing an overall translation to the south with a degree of tightening in the cluster. The longitude changes trend eastward with several events shifting westward, showing an overall translation to the east with a degree of tightening within the cluster. Changes in depth show that the depths collapsed as well. Events shallower than 5km were shifted deeper whereas events deeper than 10km were shifted shallower.

events relocated deeper with an average shift of 2.83km, implying an overall tightening of the cluster.

Figures 3.9-3.11 show cross sections of the relocation results. The cross section for subsection 1 shows a planar feature striking 76° and dipping to the south (black dashed line). The depths of the plane are collapsed sufficiently enough to show the planar structure (Figure 3.9). The cross section results for subsection 2 show an 89° striking feature that at the eastern most end has a nearly vertical dip (Figure 3.10). The cross section for subsection 3 shows two smaller regions, striking 59°, that both appear to have nearly vertical dip (Figure 3.11).

The results of both relocations show that there is a considerable degree of collapsing of the cluster onto definable features. Both relocations show a degree of translational movement; however, have an opposite sense of direction. The relocations of the entire catalog have a relative movement to the north-west, whereas the relocations of the more recent dataset show a south-east movement. One possible explanation is that when the older events were originally located, there was a bias in the location because the majority of stations used in the location were in the southeast. Since the relocation repositions the events relative to each other based on travel-time differences, this station bias was overcome. The same is true for the more recent events. The events are relocated relative to each other, and therefore, translations of the cluster are expected. The same trends in seismicity arose from both relocations which are seen not only in the map view, but also in the dips of the planar features shown in cross section. The anomalous “deep”

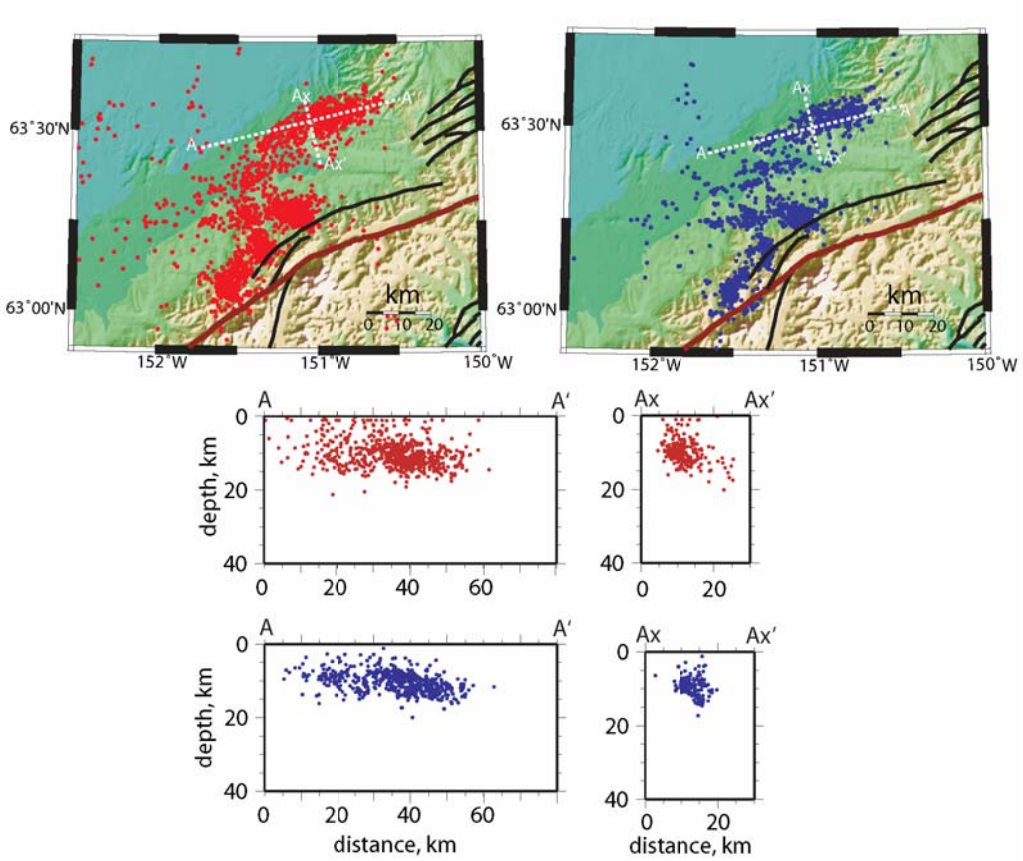

Figure 3.9 Relocation Cross Sections for the Post-2004 Events in Subsection 1. Original hypocenters are plotted in red and relocated hypocenters are plotted in blue. A cross section striking 76°, AA', shows the depths collapse into a 10km thick plane that appears to plunge to the north-east. The bisecting cross section shows the planar feature also appears to dip roughly 50° from horizontal.

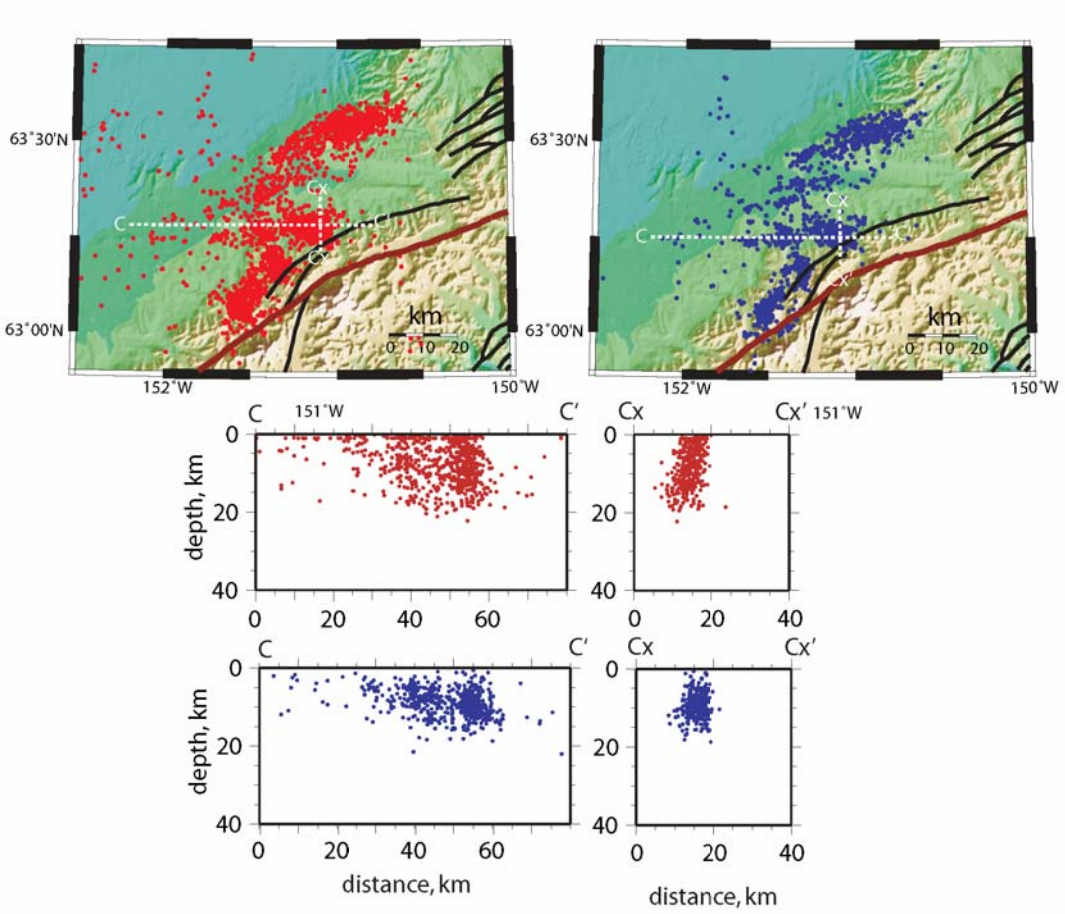

Figure 3.10 Relocation Cross Sections for Post-2004 Events for Subsection 2. The original hypocenters are plotted in red and the relocated hypocenters are plotted in blue. The cross section striking 89°, CC', shows the depths collapse onto a 10-15km thick planar feature. The bisecting cross section through the eastern portion of the subsection shows the plane to be nearly vertical.

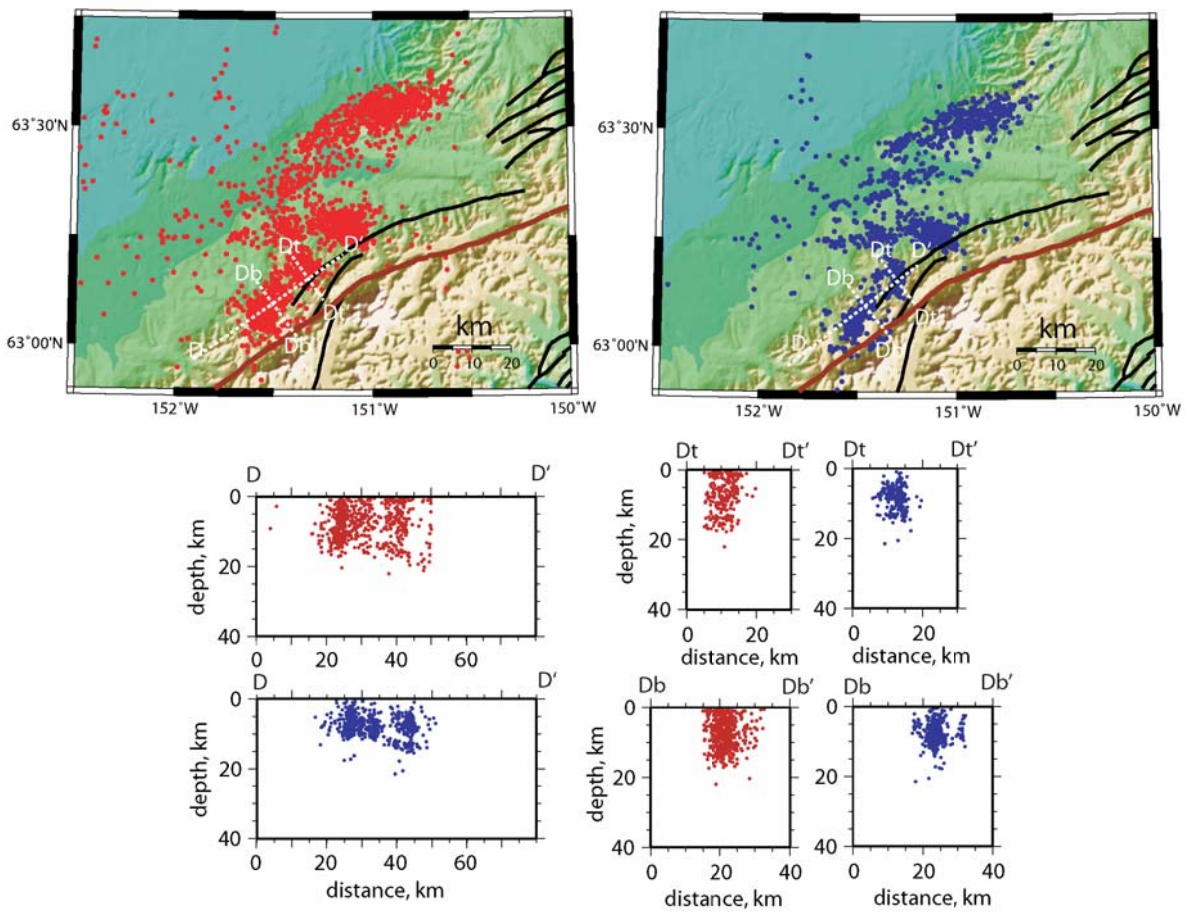

Figure 3.11 Relocation Cross Sections for Post-2004 Events for Subsection 3. The original hypocenters are plotted in red with the relocated hypocenters plotted in blue. A cross section striking 59°, DD', shows the depths collapse to reveal two separate features. Two bisecting cross sections, one through the northern portion, DtDt', and one through the southern portion DbDb', show the two features are nearly vertically dipping.

events relocated either shallower or deeper to the slab. From the relocations, smaller subsections within each larger subsection are observed. To take these smaller regions into account each subsection is then divided into two parts. Subsection 1 is divided into A and B; subsection 2 is divided into C and D; and subsection 3 is then divided into E and F (Figure 3.12). Each event is grouped into only one of the six sub-regions. The relocations results, for events with $M_L \geq 2$ and occurring after 1990, are used in chapter 4 as the preferred locations for use in calculating the seismicity rates of each subsection.

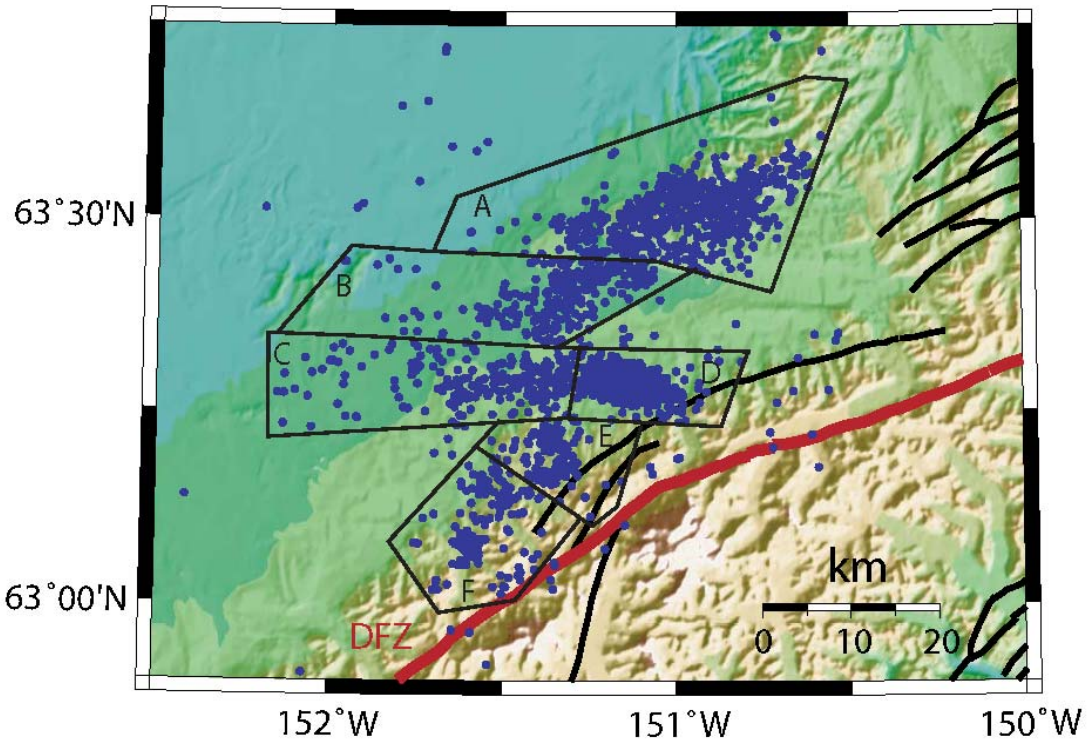

Figure 3.12 Map of the Six Smaller Sub-regions. The six smaller sub-regions resolved from the double difference relocations. Subsection 1 is broken down into sub-regions A and B. Subsection 2 is broken down into sub-regions C and D. Subsection 3 is broken down into sub-regions E and F. Each event is located in only one of the six sub-regions.

Chapter 4. Seismicity Rates

4.1 Basic Rate Calculations

The first step in seismicity rate analysis is to do a basic rate calculation, where rate equals number of events per unit time. This simple rate calculation uses a window length of 30 days (approx. one month) with an overlap of 10 days. The plot of earthquake rate shows that the rate is highly variable during the 16 year period plotted (Figure 4.1). At times, the rate reaches a maximum of 41 earthquakes per month and a minimum of zero earthquakes per month. There is a large rate increase in the mid 1990's, most likely associated with several $M_L \geq 4$ events occurring during that time interval. Figure 4.1 shows the rate with vertical lines denoting origin times of earthquakes with $M_L \geq 4$ colored according to the subsection in which the event occurred, with the purple line representing the M_w 7.9 event. Since the seismicity in the cluster appears to be influenced by larger events ($M_L \geq 4$), the catalog must be declustered to compare seismicity rates.

Declustering a catalog removes dependent events from independent events, in this case, by removing the aftershocks from the catalog (Reasenberg, 1985). Reasenberg (1985) assumes that any earthquake that occurs within the interaction zone of a prior earthquake is an aftershock and is therefore dependent on the prior earthquake. The interaction zone is defined by a look-ahead time and spatial parameters (epicentral error, depth error and scales based on source dimensions). All events classified as dependent events are replaced with one event whose origin time is that of the largest event, whose location is based on the mean of the cluster, and whose magnitude is related to the

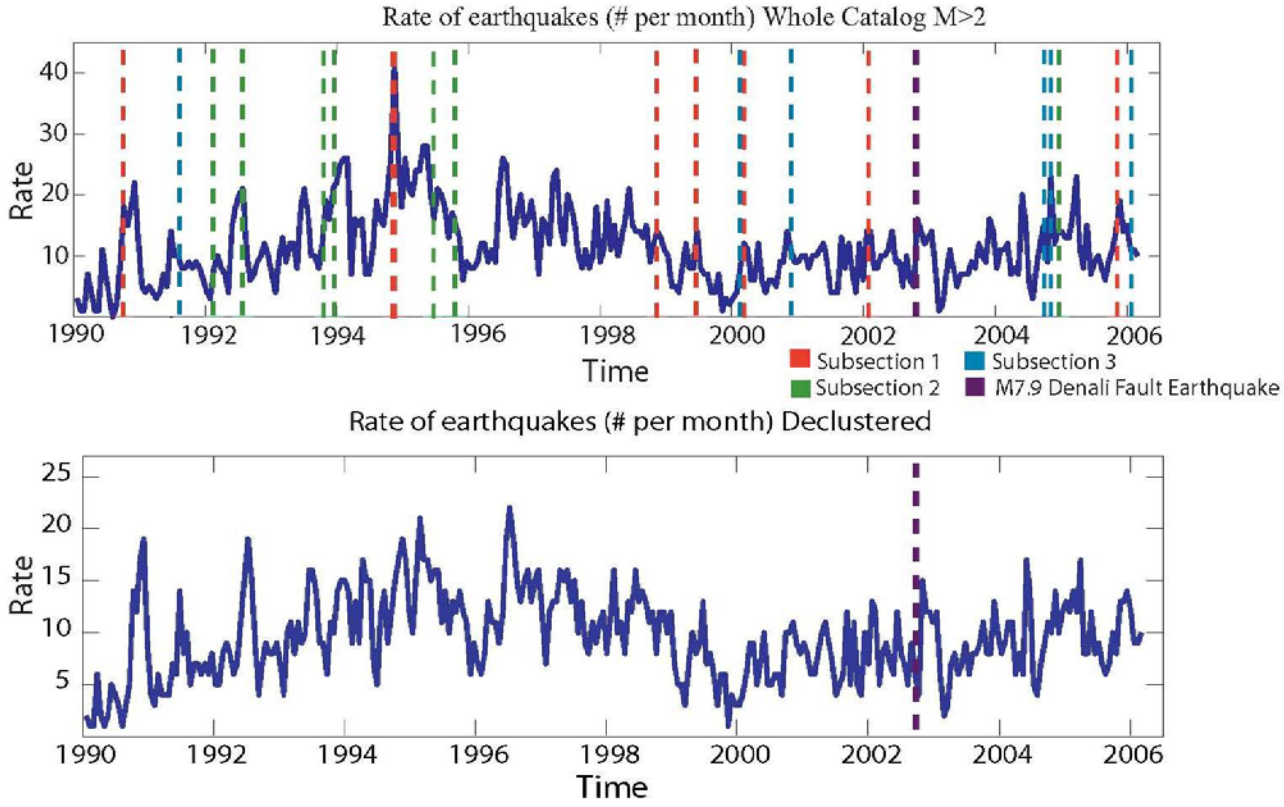

Figure 4.1 Plot of Seismicity Rate Per Month. This plot shows the number of events per 30 day window from 1990 to 2006.24. The colored lines represent events with $M_L \geq 4$, color coded by the subsection in which they occur. The bold purple line represents the occurrence of the M_w 7.9 event. A majority of the peaks in seismicity coincide with events $M_L \geq 4$. There is only a subtle increase following the M_w 7.9 event.The bottom plot shows the rate with time of the declustered catalog. Note that the same pattern emerges in the rate with the aftershocks removed.

cumulative moment of the cluster. The catalog was declustered using the method of Reasenberg (1985).

Declustering the Kantishna Cluster catalog resulted in 1895 events meeting the criteria discussed in chapter 2 (i.e. $M_L \geq 2$, and occurring since 1990). Figure 4.1 shows the rate with time of the declustered catalog compared to the original catalog. The same trends in seismicity seen in the non-declustered catalog are seen in the declustered catalog. There is a highly variable rate with time, with a period of elevated seismicity lasting through nearly all of the 1990's. The end of this period of high seismicity also coincides with the conversion to the new location algorithm mentioned in chapter 2. The high rate of seismicity is problematic when looking for changes associated with the M_w 7.9 event, because this change overshadows later changes occurring in late 2002-early 2003. To avoid potentially erroneous results, all subsequent calculations were done using both the 1990-2002.8 time period and the 1999-2002.8 time period. The data is then divided into three time periods; 1990-2002.8 (t1), 1999-2002.8 (t2) and 2002.8-2006.25 (t3).

The average rate for period t1 is 9.57 events per month, whereas the average rate for t3 is 9.05 per month. This would imply a small rate decrease coinciding with the M_w 7.9 event. However, the rate in t2 is 7.29 events per month. Comparing t2 and t3 shows an increase associated with the timing of the M_w 7.9 event.

To further define the cluster, the rates of the three subsections were also calculated using the declustered catalog (Figure 4.2). The three subsections show a peak

in rate at three different times. Figure 4.2 shows the variability in rate of each subsection with the green line representing the M_w 7.9 event. Subsection 1 shows a sharp increase in late 1994, with a high rate continuing through late 1999. The rate of earthquakes during this period of heightened activity was 5.43, with a peak at 12 events per month, whereas the average rate for t1 was only 4.39 events per month. The rates for t2 and t3 were 3.53 and 3.32 events per month respectively, implying no change coinciding with the M_w 7.9 event in subsection 1.

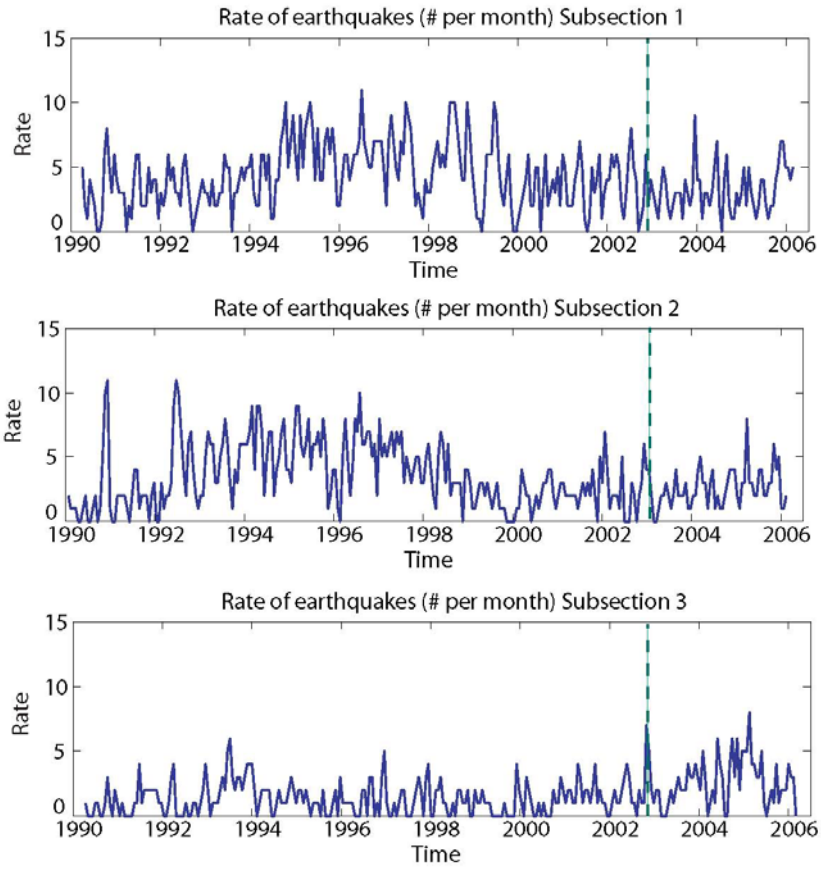

Figure 4.2 Plots of Rate for Each Subsection. The plots show the rate of earthquakes per 30 day window of the declustered catalog for each subsection 1, 2, and 3. The green line represents the occurrence of the M_w 7.9 event. Subsections 1 and 2 show very little, if any, change following the M_w7.9 event, however, subsection 3 shows a considerable increase, double that of the rate prior to the M_w7.9 event.

Subsection 2 shows a peak rate in early 1992, with a higher rate lasting through mid 1998 (Figure 4.2). The average rate from 1992 to 1999 was 4.94 with a peak of 12 events per month in April 1992. The rate in t1 was 3.61 compared to the rate in t2 of 2.15 events per month. The rate in t3 was 2.61 events per month, which is a small increase in rate compared to t2, but a decrease compared to t1.

Subsection 3 shows a fairly consistent rate until reaching a peak in late 2002. The rate then dramatically drops off and reaches another peak in 2004 (Figure 4.2). The rates for t1 and t2 were both 1.3 events per month, showing no need to separate the two. The rate in t3 was 2.7, with a peak of 8 events per month; double that of periods t1 and t2.

Figure 4.3 shows the rates of the smaller sub-regions A-F. Regions A and B both show no change in rate corresponding to the M_w7.9 event. The peak in seismicity in the mid- to late-1990s is shown in sub-region A. Sub-region C shows consistent rate throughout the time period. Sub-region D shows the peak in seismicity in the mid-1990s with no rate change coinciding with the M_w 7.9 event. Sub-region E shows a consistent rate beginning in 1993 with a slight increase beginning in early 2004. Sub-region F shows a variable rate through time with a large increase occurring in 2004.

Clearly, the seismicity in the cluster is spatially variable. This spatial variability throughout the clusters requires a more detailed look at the cluster in map view rather than as clumped subsections averaged together.

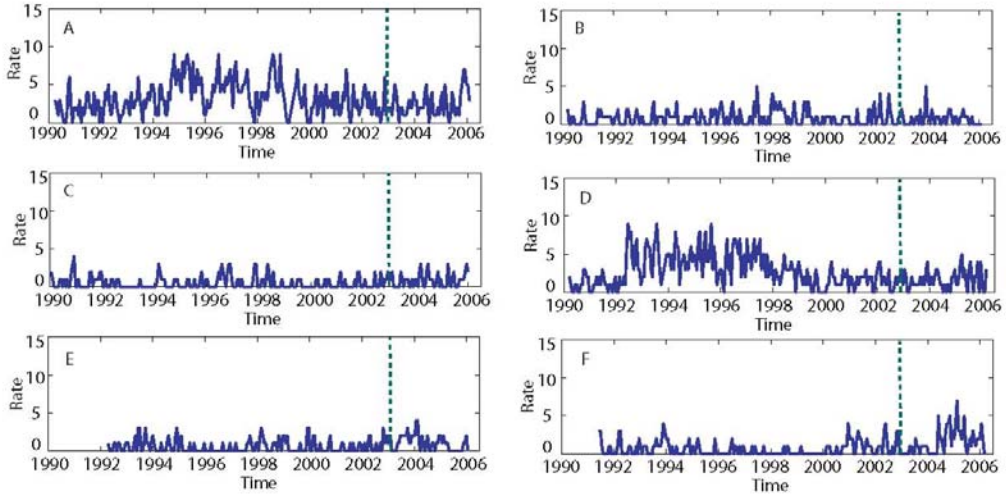

Figure 4.3 Sub-region Rates Through Time. The rates (number of events per month) of each of the six sub-regions (declustered) are plotted against time. Sub-regions D and F show a slight increase in rate following the M_w7.9 (green vertical line) as compared to the three years prior. Most sub-regions show no significant change. Sub-region F shows a noticeable increase following the M_w 7.9 event.

4.2 Z-values

A step beyond a simple rate calculations are z-values. A z-value is a measure of greatest change in rate in a catalog of earthquakes (Wyss et al., 2001). ZMAP seismicity software, developed by Stefan Weimer (Weimer, 2001), uses the Long Term Average (LTA) function to calculate the z-value. The LTA function compares the mean rate R_{all} to the mean rate R_{w1} in a window length w1 according to the following equation:

$$z(t) = \frac{(R_{all} - R_{w1})}{\sqrt{\frac{\sigma_{all}^2}{n_{all}} + \frac{\sigma_{w1}^2}{n_{w1}}}},$$

where n is the number of samples and σ is the standard deviation. The window w1 is moved over the entire data set in steps to find z as a function of time (Wyss et al., 2001). An increase in z-value represents a seismicity decrease whereas a decrease in z-value represents an increase in seismicity. Windows of 0.5, 1.0, and 1.5 years were used with no difference in the peak locations found; they simply show a difference in the smoothing of the curve (i.e. minimizes the peak amplitudes). The plot of the z-values with time is plotted against the cumulative number, where cumulative number is on the left y-axis and z-values are on the right y-axis.

The plot of z-value with time, for all events $M_L \geq 2$ in the declustered catalog, shows two peaks of seismicity increase in mid-1994 and mid-1996 with a maximum change (z minimum) of -5.2 at 1994.6. Two seismicity decreases occurred in mid-1999 and mid-2002 with a maximum change (z maximum) of 5.4 at 1999.6 (Figure 4.4). There is an abrupt decrease in z-value (seismicity increase) from 2.5 to -1, in late-2002 that continues through 2004 that is likely related to the seismicity increase in subsection 3.

Another use for z-values is a spatial map comparing two time periods. Spatial z-value maps plot z-values using a nearest neighbor approach. The nearest neighbor approach uses a user input grid of latitudes and longitudes that defines the region with equal spacing. The value at the center of each grid block created is defined by drawing a circle centered on the grid block that includes the user defined number of neighbors. The greatest change (z-value) in each block is calculated for each time period and the difference is the change in z-value. Once a value for each grid point is obtained, ZMAP assigns a color scheme according to the values, and then a map of the anomalies where

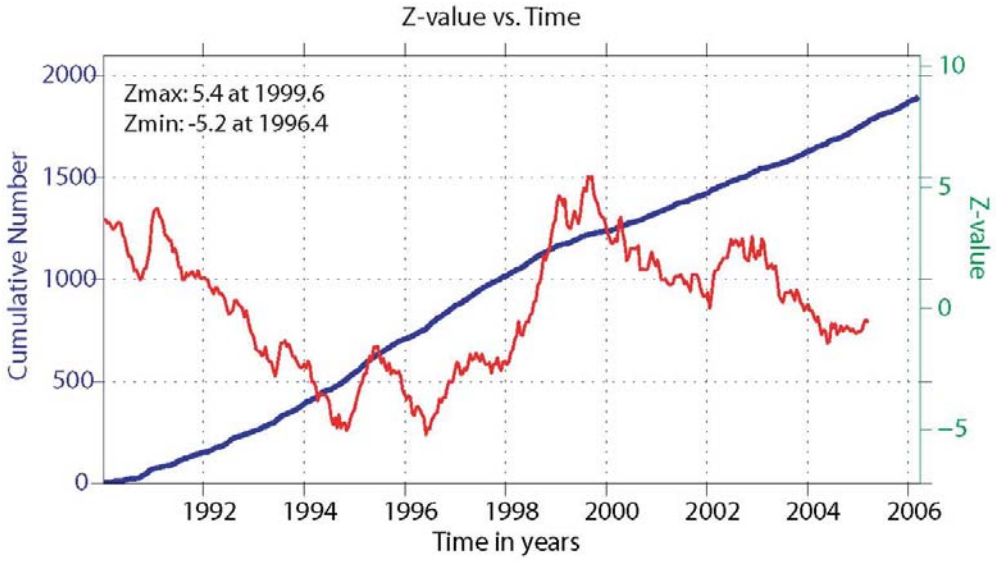

Figure 4.4 Z-Value With Time. The red line is the z-value plotted with time (window length of 1 year) of the declustered catalog. The right vertical axis shows the value of the z-value. The blue line is the cumulative number of earthquakes with time corresponding to the values in the left vertical axis. There are several periods of significant seismicity change. The two maximum are -5.2 in 1996.4 (a seismicity increase) and 5.4 in 1999.6 (a seismicity decrease).

the greatest change occurs is produced. On z-value maps the high (positive) z-values (hot colors) represent a decrease in seismicity rate, and low (negative) z-values (cold colors) represent an increase (Wyss et al., 2001). The number of earthquakes at each grid point is critical for the resolution of the map. There is a trade off between the significance of the value obtained and the resolution (Wyss et al., 2001). Few earthquakes (i.e. smaller radii) result in less significant values but a better spatial resolution. The z-value maps in Figure 4.5 use a grid spacing of 0.025 degrees in both the north-south and east-west directions, with 40 nearest neighbors. There is a considerable degree of smoothing on the edges of the maps but the internal resolution is clearer due to the increased number of earthquakes toward the centers of the subsections.

Figure 4.5 (top) shows the z-value comparison of t1 (1990-2002.8) and t3 (2002.8-2006.25) in the declustered catalog, with the epicenters of the $M_L \geq 4$ events plotted as stars and color coded by time period. From this map, it appears that a majority of the cluster experienced either a seismicity decrease or no change following the M_w7.9 event. Subsection 1 shows considerable seismicity decreases. Small regions in subsection 1 show either no change or some increase. The majority of subsection 2 was unchanged with the exception of two regions, one with an increase and one with a decrease. This corresponds well to the rates from section 4.1. Subsection 3 appears to have experienced a significant seismicity increase in the area closest to the Denali Fault.

Figure 4.5 (bottom) shows the z-value comparison of t2 (1999-2002.8) and t3. There is still a decrease in parts of subsection 1, but there is also an increase in the northern part of subsection 1 balancing out the rates shown in Figure 4.2 and 4.3 (section 4.1), giving the overall subsection zero change. Subsection 2 shows an overall small increase in seismicity with the center most area showing zero to minimal decrease. The small rate increase shown here correlates well with the rates observed in section 4.1. Subsection 3 shows an increase over the full subsection, which corresponds well with the rates in section 4.1.

Comparing both maps in Figure 4.5, three areas of seismicity increase/decrease are apparent. The southern part of subsection 1 shows an overall decrease despite the rate fluctuations that arose in section 4.1. The northernmost part of Subsection 1 shows a seismicity increase. Both imply a definite change that corresponds in time with the M_w7.9 event. The same is observed in subsection 3, where there is an overall seismicity increase

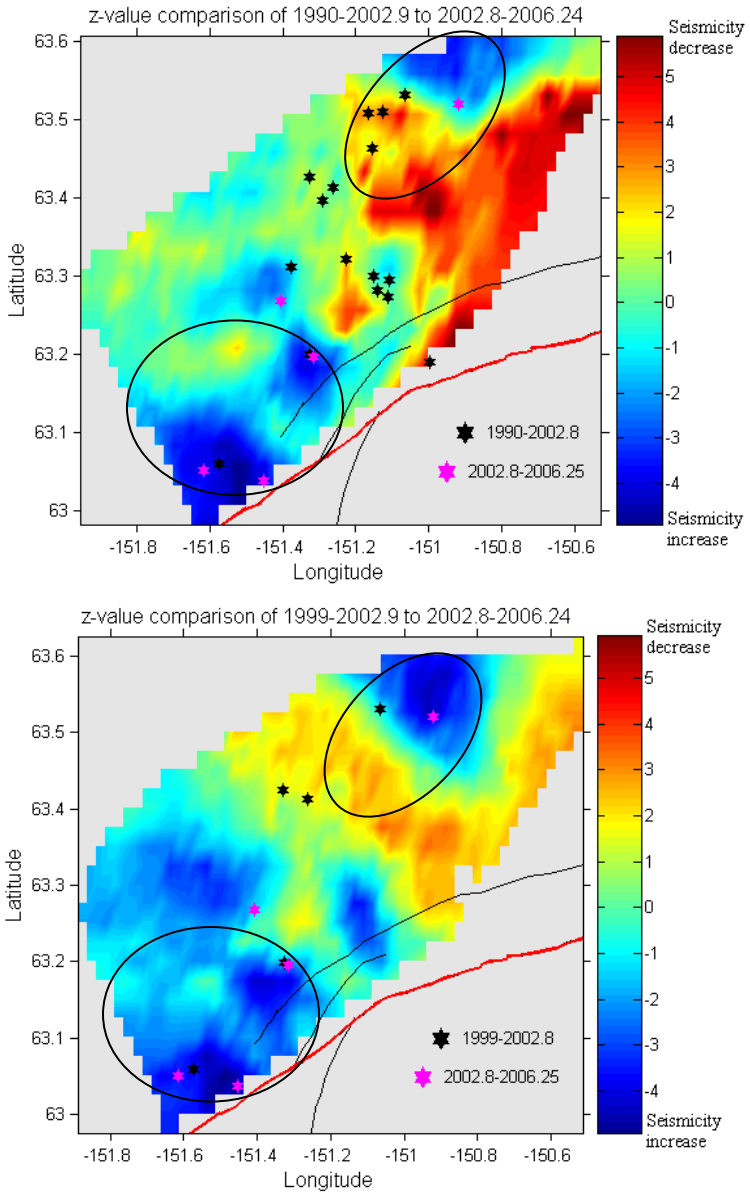

Figure 4.5 Z-value Maps. Top: Map of changes in z-value of the declustered catalog comparing the two time periods 1990-2002.8 and 2002.8-2006.24. Bottom: Map of changes in z-value of the declustered catalog comparing the two time periods 1999-2002.8 and 2002.8-2006.24. The black lines represent the faults in the region, with the red line representing the Denali Fault. The colors represent the change in z-value in each grid spacing. Note positive changes represent decreases in seismicity. The stars represent the $M_L \geq 4$ events in the Kantishna Cluster. The circles mark the regions of similar change between the two regions. These changes appear to be independent of the time interval used and may correspond directly in time to the M_w7.9 event.

corresponding to the time of the M_w7.9 event. Although the seismicity changes are not to the same extent in both time comparisons, they do exist independent of any bias between the two time periods.

4.3 B-values

Another method for calculating seismicity rates is the b-value. The b-value defines the relationship between frequency of earthquakes and magnitude. The b-value is found by plotting the frequency magnitude distribution and fitting a line to the curve that satisfies the following equation;

$$\log_{10} N = a - bM,$$

where M is magnitude, N is the cumulative number of earthquakes with magnitudes greater than M, and a and b are constants, known as the Gutenberg-Richter relation (Gutenberg and Richter, 1944). The best fit line to the frequency magnitude distribution is found using a standard weighted least squares method. The slope of the line, b, is the b-value. The b-value gives the relative relationship of large versus small events. Laboratory experiments have shown that b-value increases with increases in heat, pore pressure and material heterogeneity and decreases with applied stress (summarized in McNutt, 2002).

Plots of the b-values in the Kantishna Cluster for t1 (1990-2002.8) compared to t3 (2002.8-2006.25) show that the b-value drops from 0.993±0.04 to 0.884±0.02. A drop of 0.1 would indicate more larger events relative to smaller events conducive with the

application of stress (Figure 4.6 top). When comparing t2 (1999-2002.8) to t3 (2002.8-2006.25), the b-values are similar, 0.893±0.06 and 0.884±0.02 respectively (Figure 4.6 bottom). The large uncertainty for t2 shows that the b-value could potentially be as high as t1 or as low as t3. To better understand temporal changes, spatial calculations were also done.

Unlike temporal plots of b-values, spatial b-value plots give insight into the distribution of b-value changes. The same nearest neighbor approach used in z-value maps is used in b-value maps (section 4.2). The same 40 neighbors and 0.025 degree grid spacing as in section 4.2 were used. B-value maps represent either individual time intervals or the difference between two time intervals (delta b). Figure 4.7, shows the differential b-value maps comparing t1 to t3 (top), and t2 to t3 (bottom). Hot colors represent positive changes, meaning an increase in smaller events relative to larger events, and cold colors represent negative changes.

Figure 4.7 (top), shows an overall small decrease in b-value. Intermittently, there are areas of very small b-increases and decreases. The noteworthy areas of the b-value map are the area of high b-value change in subsection 1 and the center of subsection 2. The area in subsection 1 shows an increase in b-value of 0.4, meaning an increase in smaller events with respect to larger events, possibly associated with a decrease in applied stress. This area matches up well with an area in the z-value maps of a seismicity decrease (Figure 4.5 top). The center of subsection 2 shows a considerable decrease of 0.8, meaning a decrease in smaller events to larger events. This area also matches up with a seismicity decrease in the z-value maps (Figure 4.5 top).

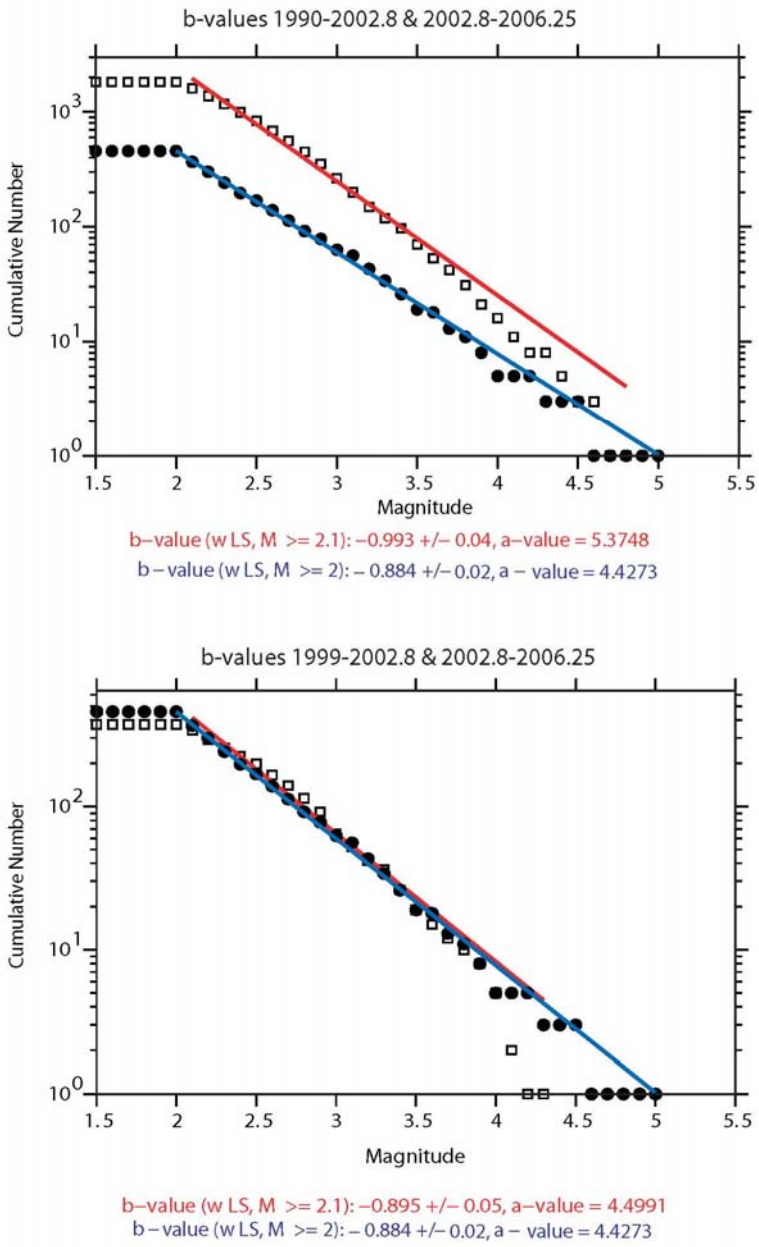

Figure 4.6 B-value Plots. Top: b-value plot comparing 1990-2002.8 (white boxes) to 2002.8-2006.25 (black dots). Bottom: b-value plot comparing 1999-2002.8 (white boxes) to 2002.8-2006.25 (black dots). The red lines represent the b-values for the two time periods before 2002.8 and the blue line represents the b-value after 2002.8. The plot showing 1990-2002.8 versus 2002.8-2006.25 shows there is a significant decrease in b-value in 2002.8-2006.25. The plot showing 1999-2002.8 versus 2002.8-2006.25 shows within the margin of error no change in b-value.

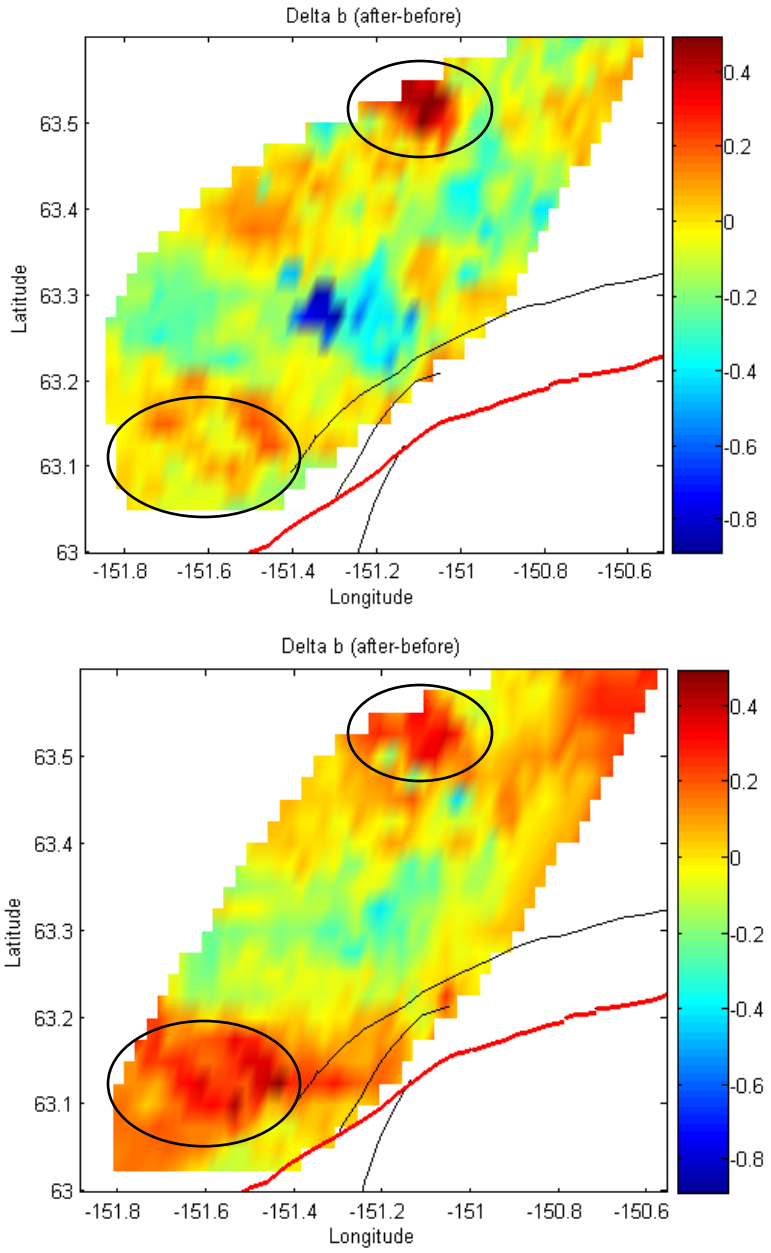

Figure 4.7 B-value Maps. Top: b-value map comparing 1990-2002.8 to 2002.8-2006.24 showing changes in b-value between the two time periods. Bottom: b-value map comparing 1999-2002.8 to 2002.8-2006.25, showing the changes in b-value between the two time periods. In b-value maps, increases in b-value show an increase in smaller events relative to larger events. The black circles highlight regions where change in common in both maps. These changes appear to be independent of the time interval used and may correspond directly in time to the M_w7.9 event.

Figure 4.7 (bottom), is the b-value comparison of t2 with t3. Overall, the mapped region shows, within the margin of error, no change. The noteworthy areas of this map include subsection 3, where there is an increase in b-value, and the same area of subsection 1 as in Figure 4.7 (top), where there is still a b-value increase. The presence of the positive b-value change in both the maps implies a definite change in b-value corresponding in time to the M_w7.9 event. The absence of the subsection 2 decrease in the t2/t3 comparison implies the b-value change is closer linked in time to the rate changes occurring in the mid-1990's than the occurrence of the M_w7.9 event. The positive change in subsection 3 can be seen, although subtly in the t1/t3 delta b map, implying that the change is potentially linked in time to the M_w7.9 event.

Overall, the cluster as a whole does not appear to have many changes associated with the M_w 7.9 event. Only when broken down into discrete subsections are any significant changes observed. Subsection 1 experienced a very small decrease (0.2 events per month) in overall rate when comparing the 3.8 years prior to the M_w 7.9 event to the 3.25 years following. Subsection 1, however, showed areas of increased z- and b-values that were balanced out by areas where both values decreased. Subsection 2 showed a slight increase (0.5 events per month) in overall rate comparing the 3.8 years prior to the M_w 7.9 event to the 3.25 years following. The z-value decreased slightly, implying a slight seismicity increase with no significant change in b-value. Subsection 3 showed the most dramatic changes. The overall rate more than doubled. The z-value decreased substantially (seismicity increase) and the b-value increased as well implying a decrease in applied stress. The lack of a clear background pattern in the years preceding the

M_w7.9 event make comparisons in time difficult. The highly variable background rate in subsections 1 and 2 tends to mask any changes potentially related to the M7.9 event. Subsection 3, however, has a very stable background and shows clearly the influence of the Denali Fault earthquake.

Chapter 5. Stress Changes

5.1 Fault Plane Solutions

In addition to assessing the seismicity rates, this study examined the stresses and stress changes in the cluster. Ratchkovski (2001) found that most earthquakes in the Kantishna Cluster are characterized by reverse faulting, ranging from pure thrust mechanisms to strike-slip with a significant reverse component. Prior to the M_w 7.9 event, the catalog of fault plane solutions is nearly complete to M_L 3.0 (63 events). After the M_w 7.9 event, the catalog is only complete to M_L 3.5. Routine processing at the AEIC calculates fault plane solutions for earthquakes M_L 3.5 and greater in Alaska, and earthquakes down to M_L 3.0 were added manually using the program FPFIT (49 events). Events with magnitudes less than 3.0 were not used, because the events were small enough that fifteen clear first motions, the minimum number required for FPFIT, or good coverage of the focal sphere could not be found.

FPFIT is a program that finds the double-couple fault plane solution that best fits a given set of observed first motion polarities for an earthquake (Reasenberg and Oppenheimer, 1985). The inversion is accomplished by a two-stage grid-search procedure that finds the source model that minimizes a normalized, weighted sum of first motion polarity discrepancies. The solutions (strike, dip, and rake) are plotted on a lower hemispheric projection and the values are put back into the catalog for use in other calculations. Figure 5.1 shows the distribution of all lower hemispheric projection focal mechanisms used in the following stress tensor inversions in the Kantishna Cluster. The two smaller maps in Figure 5.1 show the focal mechanisms for events occurring between

1990 and the M_w7.9 event (labeled Before) and events occurring after the M_w7.9 event (labeled After). The colored regions of the focal mechanisms represent the compressional quadrant and are colored based on depth, red representing 0-10km depths, light blue representing 10-20km depths and dark blue representing 20-60km depths .

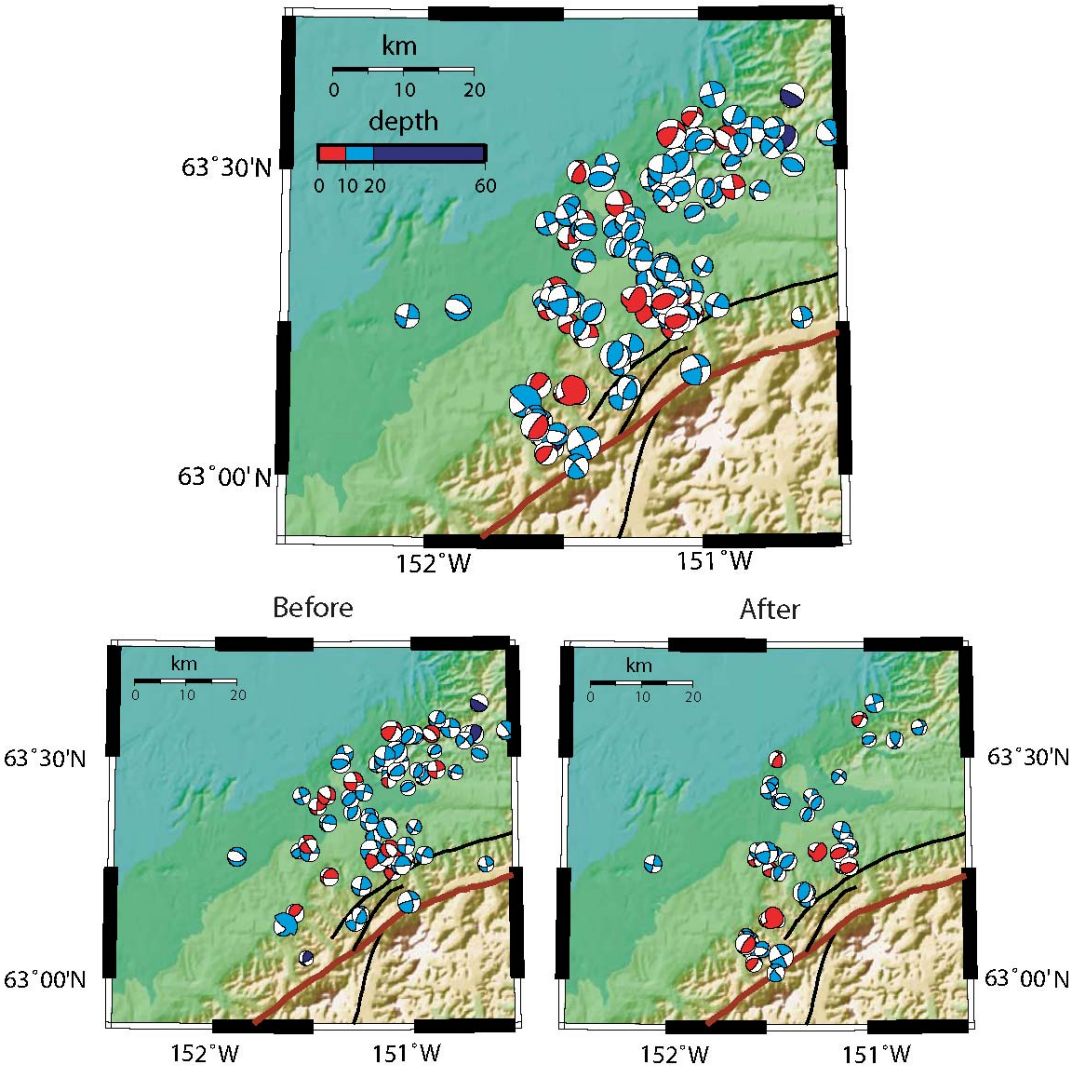

Figure 5.1 Map of Focal Mechanisms Used in Stress Tensor Inversions. The top map shows all events in the Kantishna Cluster with focal mechanisms ($M_L \geq 3$). The beach balls are colored by depth and sized by magnitude. The bottom maps show the events occurring before 2002.8 (left) and events occurring after 2002.8 (right).

5.2 Stress Tensor Inversions

The stress tensor inversions use the method of Michael (1984). The basis of the inversion is that the tangential traction (or tangential component of the friction) on the plane tends to be parallel to the slip direction,

$$\hat{\tau} = \frac{\bar{\tau}(\hat{n}, \sigma)}{\left|\bar{\tau}(\hat{n}, \sigma)\right|} = \hat{s},$$

where $\bar{\tau}(\hat{n}, \sigma)$ is the tangential traction on the fault plane with the unit normal $\hat{n}$, due to the deviatoric stress tensor σ, and $\hat{\tau}$ is the unit vector associated with $\bar{\tau}$ (Michael, 1984). Combining the equation for tangential traction with the assumption that the isotropic stress is zero, a vector containing the stress tensor elements is derived. It is necessary to solve this equation simultaneously for multiple faults to find a single σ (deviatoric stress tensor) that best satisfies all of the faults. Confidence region estimations of the solution use a bootstrap approach with 2000 iterations (Wyss et al., 2001). By bootstrapping, errors in the data can be ignored without making assumptions about the dataset. The inversion is run for each bootstrap iteration, and a normalized scalar product is used to estimate the 95% confidence regions (Wyss et al., 2001). These confidence regions are used to calculate the variance (or spread) of the inversions results. Once the stress tensor is known, the principle stresses and directions are calculated and displayed in a lower hemispheric stereographic projection.

The data were broken down into the following groups: events before the M_w7.9 event (2002.8), events after 2002.8, and events occurring in each subsection before 2002.8 and after 2002.8. Table 5.1 shows the number of events used in each inversion.

Table 5.1. Number of Events Used in Each Inversion.

Inversion	Before 2002.8	After 2002.8
Entire Cluster	63 events	49 events
Subsection 1	36 events	15 events
Subsection 2	19 events	16 events
Subsection 3	8 events	18 events

Figure 5.2 shows the results from the inversion of data before and after 2002.8 for the entire cluster. Figure 5.2 shows the results of each bootstrap iteration along with the best fitting inversion result. To the right of each inversion result is a beach ball schematic representation. The colored region represents the compressive quadrants. Also shown are the variance, faulting type, and trend and plunge of the principle stress axes. Looking at the cluster as a whole, shows that the overall stress in the cluster changed from predominately strike-slip to having more of a thrust component. The axis of maximum compressive stress (P-axis) stayed the same, but the axis of minimum compressive stress (T-axis) shifted closer to vertical. Ratchkovski (2001) showed a single stress tensor inversion is not appropriate for the Kantishna Cluster. The stresses are highly variable throughout the region.

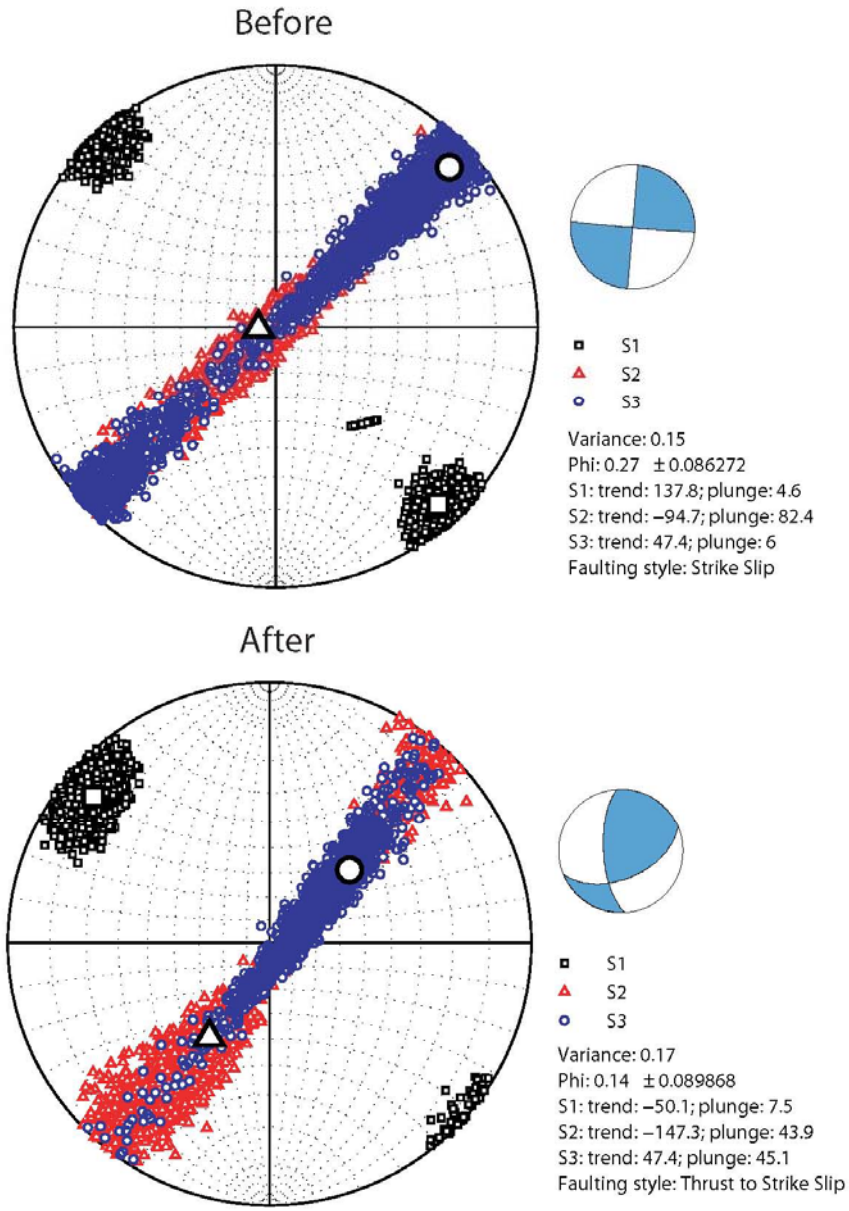

Figure 5.2 Stress Tensor Inversions for the Entire Cluster Before and After the M_w7.9 Event. Top: Best fitting stress tensor for the Kantishna Cluster prior to 3 November 2002. Bottom: Best fitting stress tensor for the cluster after 3 November 2002. Plotted with the stress tensor result is a focal mechanism schematic of the results. The maximum compressive stress results are plotted as black squares. The minimum compressive stress results are plotted as blue circles. Comparing the two results, the maximum compressive stress remains the same; however, the minimum compressive stress moves closer to vertical implying a shift to more of an obliquely thrusting environment.

Taking into account the spatial variability of the Kantishna Cluster, inversions were done for each subsection. Figure 5.3 shows the result of the inversions for each subsection with events occurring before 2002.8 and Figure 5.4 shows the result of the subsection inversions for events after 2002.8. Next to each inversion result is plotted a beach ball representation of the inversion result as well as the trend and plunge of each principle stress axis. The subsection inversions show that the P-axis orientation changes in each subsection. The P-axis orientation rotates counter-clockwise from subsection 1(north) to subsection 3(south) as highlighted in Figure 5.5. Overall, the P-axis showed no change in any of the three subsections when comparing before 2002.8 to after. The comparison of the inversions for subsection 1 before and after 2002.8 shows a change from predominately strike-slip to an oblique slip with a thrust component. Subsection 2 also shows a change from predominately strike-slip to obliquely slipping with a thrust component. Subsection 3 shows no change when comparing before 2002.8 to after.

In addition to comparing the different time periods, inversions for all events in each of the six sub-regions were done (Figure 5.6). Comparisons with time were not calculated for the smaller sub-regions because of the small number of the events within the sub-regions. Looking at the overall picture of the Kantishna Cluster will give more insight into the stress environment throughout the cluster.

The same overall trends in P- T- and N-axes as in the subsection inversions are seen in the sub-region inversions. The maximum compressive stress axes rotate counter-clockwise from north to south.

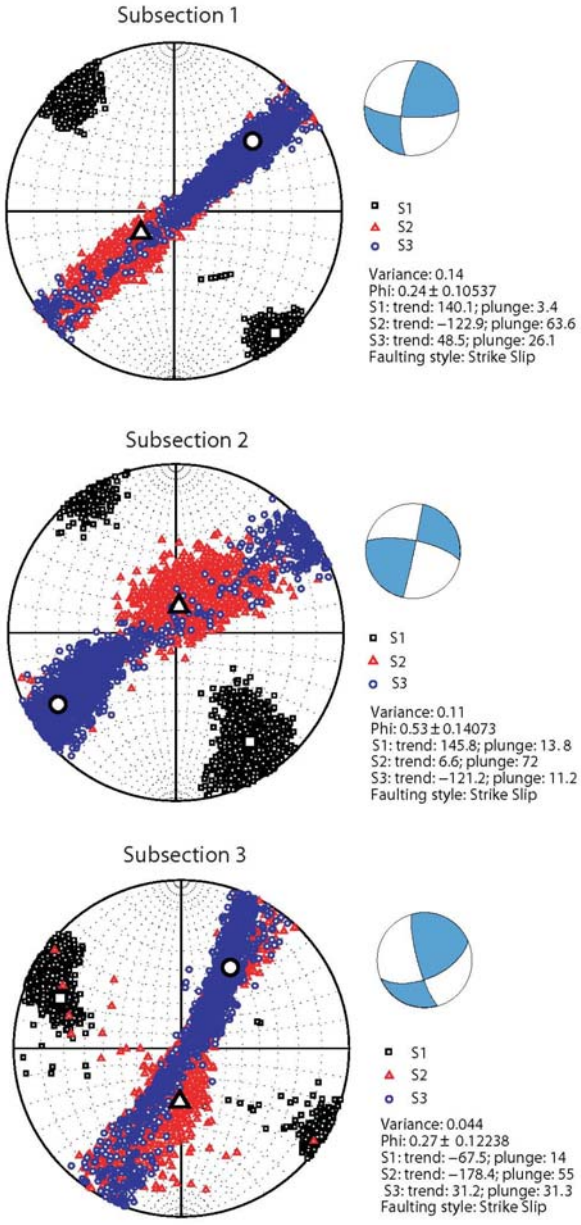

Figure 5.3 Stress Tensor Inversion Results for Each Subsection Before 2002.8. Subsections 1, 2, and 3 are plotted showing the best fitting stress tensor for each region. Plotted along with each inversion result is a focal mechanism schematic representation of the result. The maximum compressive stress results are plotted as black squares. The minimum compressive stress results are plotted as blue circles. The maximum compressive stress appears to rotate counter clockwise from north to south through the cluster.

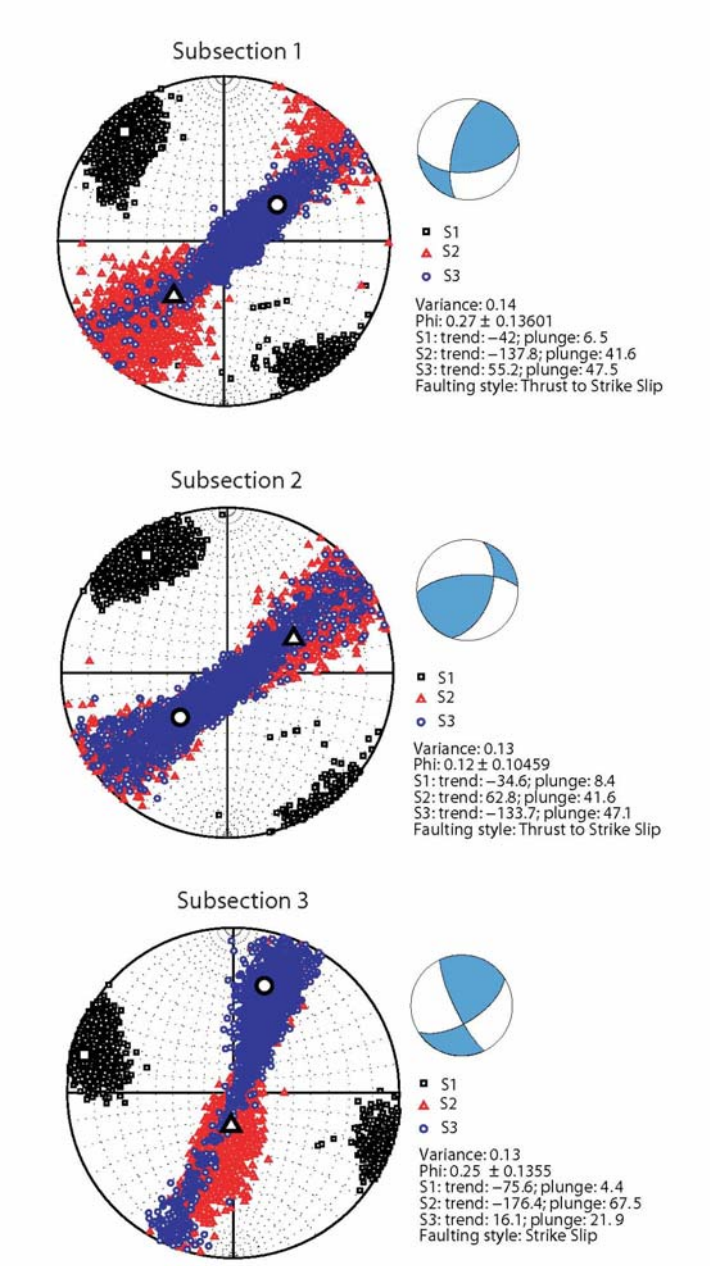

Figure 5.4 Stress Tensor Inversion Results for Each Subsection After 2002.8. Subsections 1, 2, and 3 are plotted showing the best fitting stress tensor for each region. Plotted along with each inversion result is a focal mechanism schematic representation of the result. The maximum compressive stress results are plotted as black squares. The minimum compressive stress results are plotted as blue circles. The maximum compressive stress continues to rotate counter-clockwise from north to south. In subsections 1 and 2, the minimum compressive stress shifts towards vertical becoming more obliquely thrusting, while subsection 3 remains strike-slip.

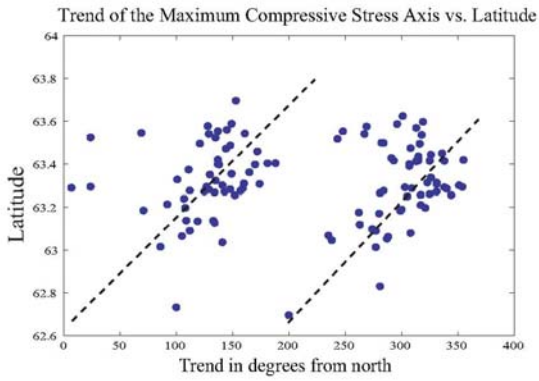

Figure 5.5 Plot of P-axis Trend Versus Latitude. This plot shows the rotation of maximum compressive stress axis (P-axis). There is a noticeable rotation counterclockwise moving from north to south through the cluster. The p-axis trend is plotted in degrees from north.

A stress map of the cluster could not be calculated due to the small number and spatial distribution of the events with fault plane solutions. Figure 5.7 shows the relocated hypocenters with the focal mechanism representing each sub-region plotted at its center. The colored lines represent the strike of each of the inferred planes found from seismicity trends as a result of the hypocentral relocations. The cross sections are taken along strike and perpendicular to strike of the seismicity trends in the direction of the arrow. The stresses resolved from the stress tensor inversions match reasonably well with the fault planes inferred from seismicity trends (Figure 5.7). The results of the stress tensor inversions are used to propose motion directions on the inferred faults. Table 5.2 shows the strike, dip and length of the inferred fault planes.

Table 5.2 Strike, Dip, and Length Of Inferred Fault Planes Resolved from Hypocentral Relocations.

Sub-region	A	B	C	D	E	F
Strike (from N)	76	19	90	115	350	59
Dip (from hz)	50	90	90	90	50	90
Length (km)	50	12	18	15	10	10

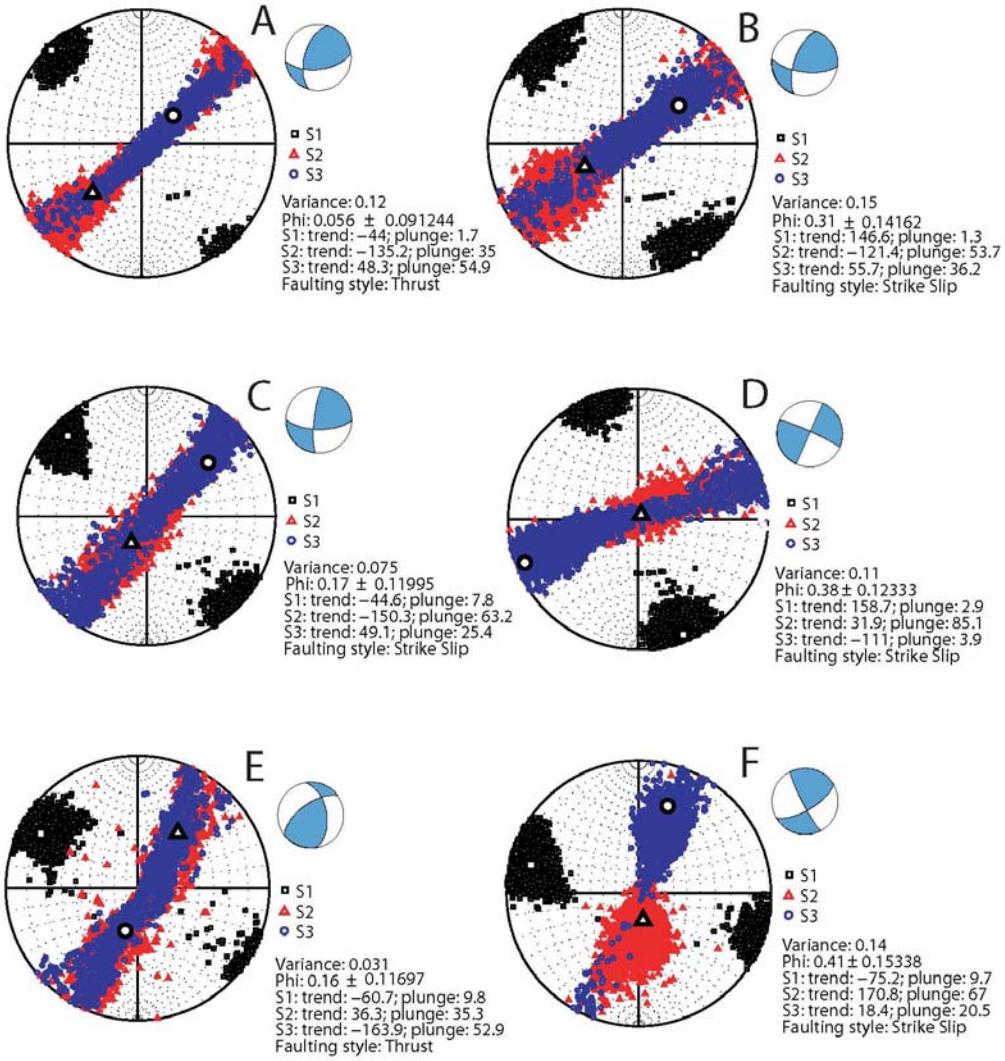

Figure 5.6 Stress Tensor Inversions For Each Sub-region. The stress tensor inversion results for each of the smaller sub-regions of each subsection are shown above. The letters correspond to the map in Figure 3.12. Along with each stress tensor inversion is a beach ball schematic representation of the inversion result. The maximum compressive stress results are plotted as black squares. The minimum compressive stress results are plotted as blue circles. The same counter-clockwise rotation of the maximum compressive stress seen in Figures 5.3 and 5.4 is seen here.

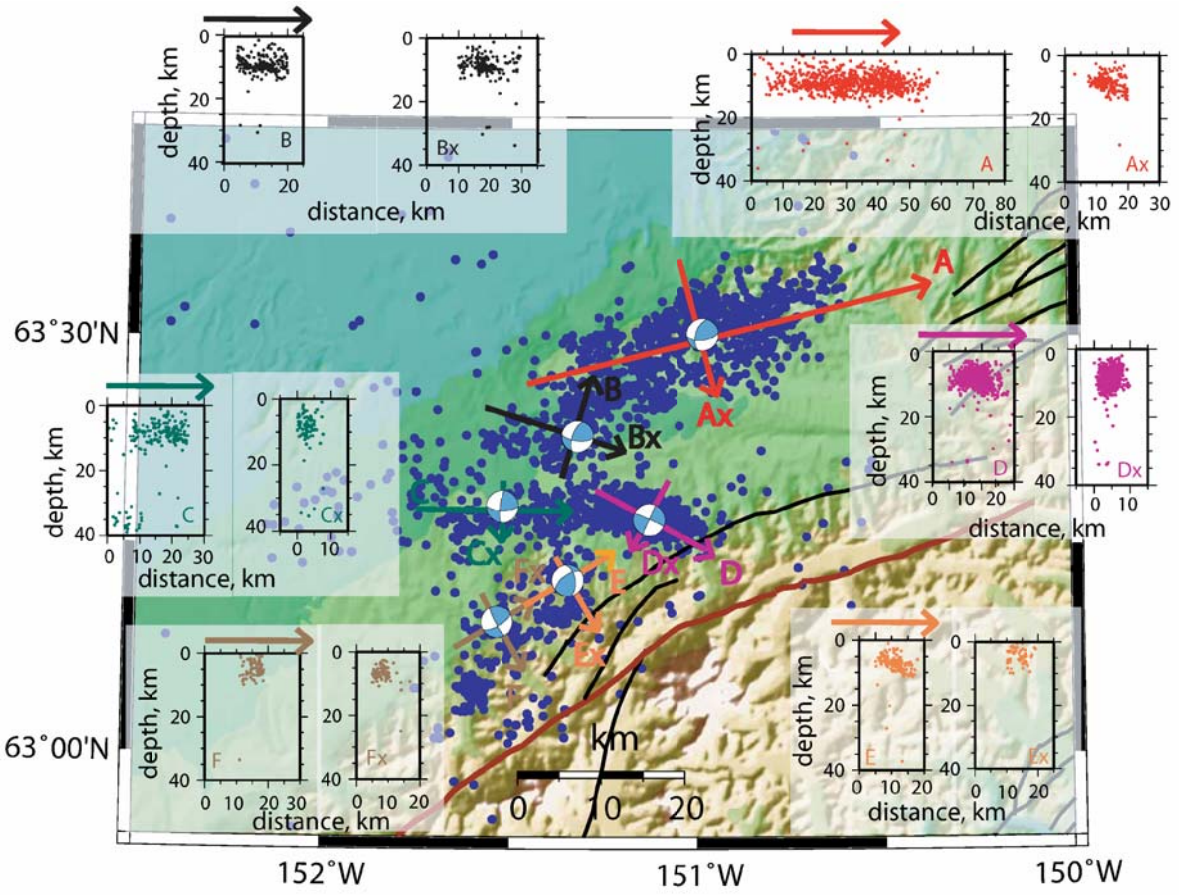

Figure 5.7 Map with Cross Sections Of Seismicity Trends Shown with Stress Tensor Inversion Results. The results of the stress tensor inversions are plotted on top of the results from the hypocentral relocations and cross sections corresponding to the inferred fault planes resulting from the hypocentral relocations are shown. The cross sections strike in the direction of the arrow. The stress tensor inversions match reasonably well with the inferred planes.

Figure 5.8 shows a schematic representation of the inferred fault planes (resolved from seismicity trends) with the maximum compressive stresses (black arrows) plotted for each sub-region. The triangles shown in sub-region A (red) and sub-region E (brown) represent thrust motion. The arrows point towards the hanging wall. The inset figure shows a three dimensional representation of the inferred fault planes. The colors on the inset correspond to the inferred faults in the map. Figure 5.8 shows a first look at the complicated geometry of the Kantishna Cluster.

Stress tensor inversion results alone do not completely describe the seismicity in the Kantishna Cluster. In section 5.3, the break down of mechanism types within the cluster are discussed and compared to the inversion results.

5.3 Focal Mechanism Triangle Diagrams

A stress tensor inversion gives the best fitting orientation of stresses in the region, but plotting the earthquakes by type shows the diversity within the cluster. To plot earthquakes by type, a ternary plot, or triangle diagram, is used. Triangle diagrams are simply a quantitative method for graphically displaying the dip angles for focal mechanisms (Frohlich, 1992). The vertices of the triangle represent normal, thrust, and strike-slip mechanisms. The colored lines on the plots represent dip angles greater than 60° for strike-slip (blue) and normal mechanisms (red), and angles greater than 50° for thrust mechanisms (green) (Frohlich, 1992). Figure 5.9 shows the triangle diagram representation of all events in the Kantishna Cluster with fault plane solutions (i.e. those used in the inversions). The trend and plunge of the P-, T-, and N-axis for each event are

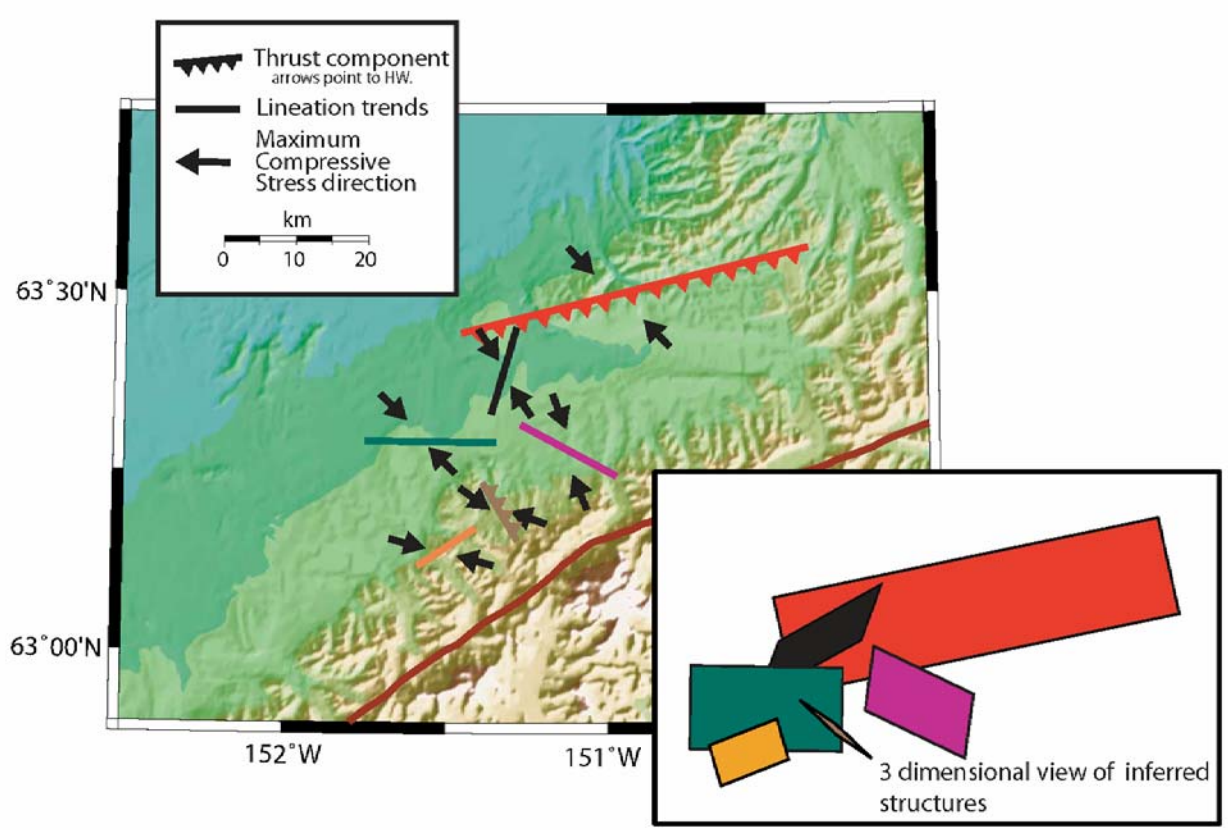

Figure 5.8 Schematic of Motion for the Inferred Fault Planes. The fault planes inferred from seismicity trends are shown here. The teeth on the fault plane represent thrust motion. The teeth point toward the hanging wall. The black arrows show the maximum compressive stress direction. The dark red line shows the Denali Fault. The inset shows a three dimensional view of the inferred fault planes. The rotation of maximum compressive stress is seen clearly.

plotted on a lower hemispheric stereographic projection. The P-axes are similar and tend to spread from 90° to 180° and from 270° to 360° from north with very shallow plunges. The T-axes tend to fall between 0° to 90° and 180° to 270° from north with highly variable plunges. There is a significant degree of scatter associated with the N-axes. The

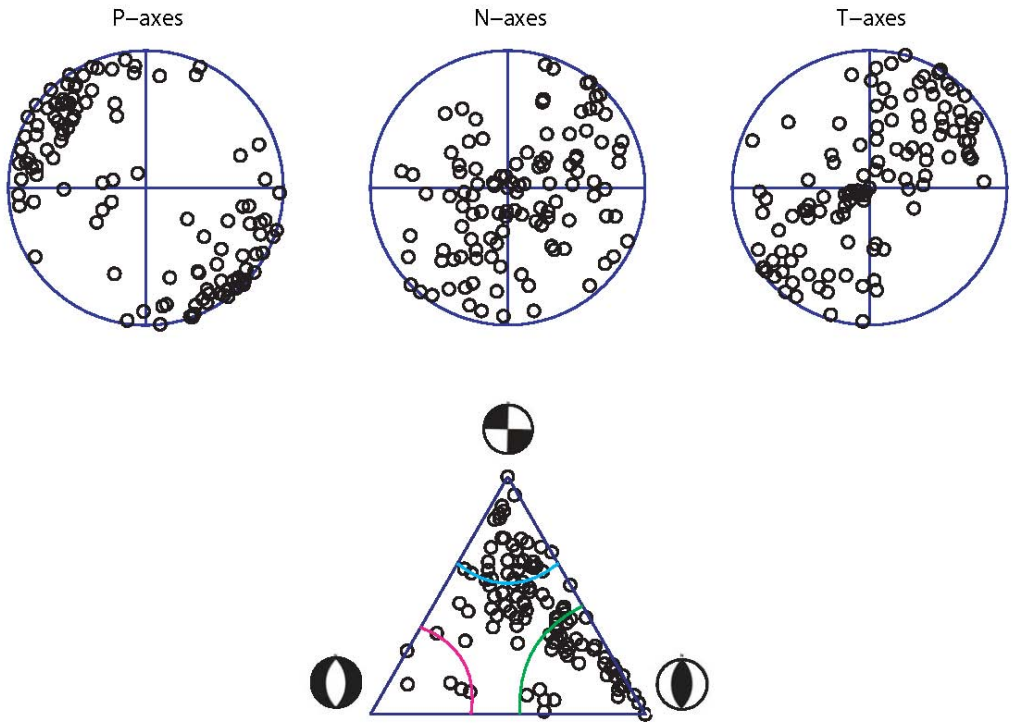

Figure 5.9 Triangle Diagram for all Focal Mechanisms. The circles show the distribution of P-, T-, and N-axes for all earthquakes with fault plane solutions. The triangle diagram shows the distribution of mechanism types for all earthquakes. The colored bands represent the defining boundaries for standard strike-slip, reverse, and normal mechanisms. The vast majority of Kantishna Cluster events fall between purely strike-slip and purely thrust/reverse type events. There are several events that have normal mechanisms. The P-axes are generally shallow dipping and between 90°-180° and 270°-360° from north. The T- and N-axes are distributed through out the focal sphere.

triangle diagram shows that every mechanism from pure thrust to pure strike-slip is present within the Kantishna Cluster. Several normal mechanisms are also present, again showing the overall complexity of the faulting in the cluster.

Figure 5.10 shows the comparison of mechanisms occurring before 2002.8 and after 2002.8 for the whole cluster. The distribution of mechanisms is nearly the same, although fewer normal events occurred after 2002.8. The trends in P- T- and N- axes remain relatively similar between the two time periods, despite the stress tensor inversion showing a change from strike-slip to oblique thrust (section 5.2).

The events are then broken down into subsections with the triangle diagram representations shown in Figure 5.11. The first column shows triangle diagrams for events before 2002.8. The second column shows the diagrams for events after 2002.8. The third column shows all events before and after 2002.8. Subsection 1 has twice the number of events before than after. The general trend of the events appears the same but an accurate comparison is difficult with such a small number of events. There are no normal faulting events, and the overall trend after 2002.8 is obliquely thrusting. Subsection 2 has roughly the same number of events to compare. There are no normal faulting events after 2002.8, and the distribution changes slightly from having more strike-slip to having more obliquely thrusting events. This distribution matches well with the inversion result for subsection 2 from section 5.2. Subsection 3 has over twice the number of events after 2002.8 than before. The events are more distributed around the triangle. With the difference in number of events, an accurate comparison is difficult in subsection 3.

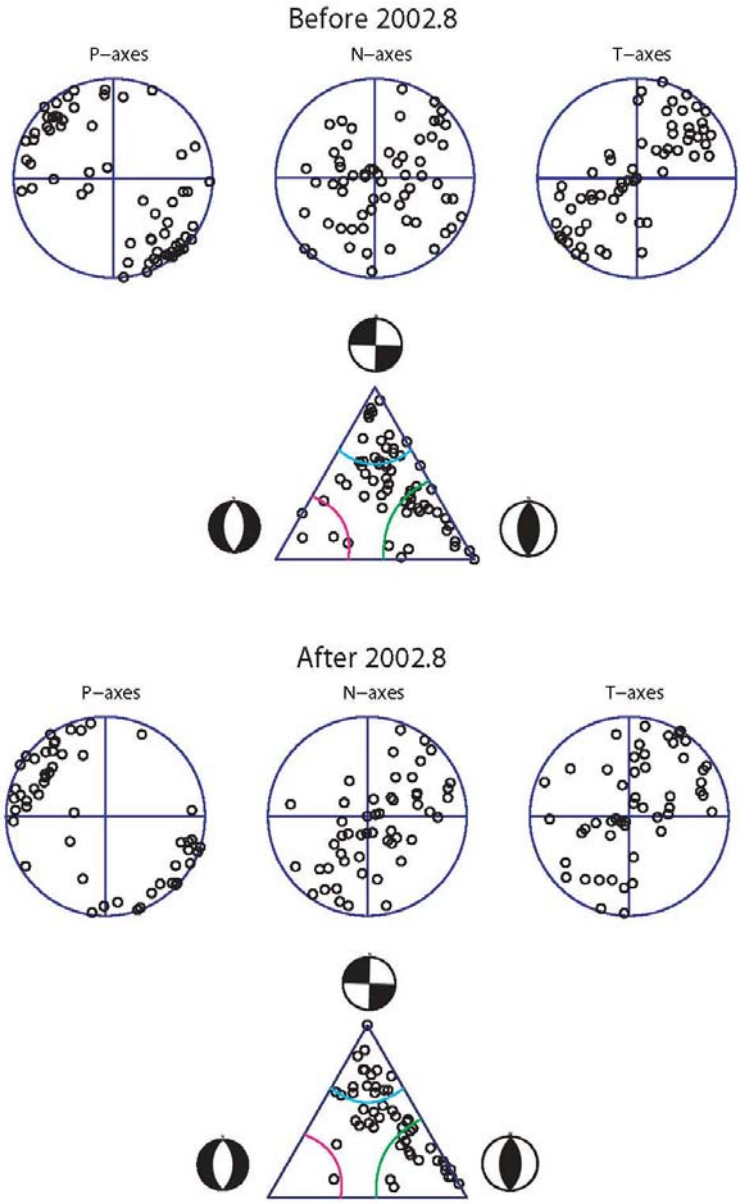

Figure 5.10 Triangle Diagrams for Before and After 2002.8. Top: Triangle diagram for focal mechanisms before 2002.8. Bottom: Triangle diagram for mechanisms after 2002.8. The colored bands represent the defining boundaries for standard strike-slip, reverse, and normal mechanisms. The circles in both represent the distribution of P-, T-, and N-axes within the respective time periods. The triangle diagrams show the distribution of mechanism types within each time period. The distribution before and after 2002.8 shows that although the stress tensor inversion shows the region becoming more obliquely thrusting, the mechanisms remain quite similar, with fewer normal faulting events after 2002.8.

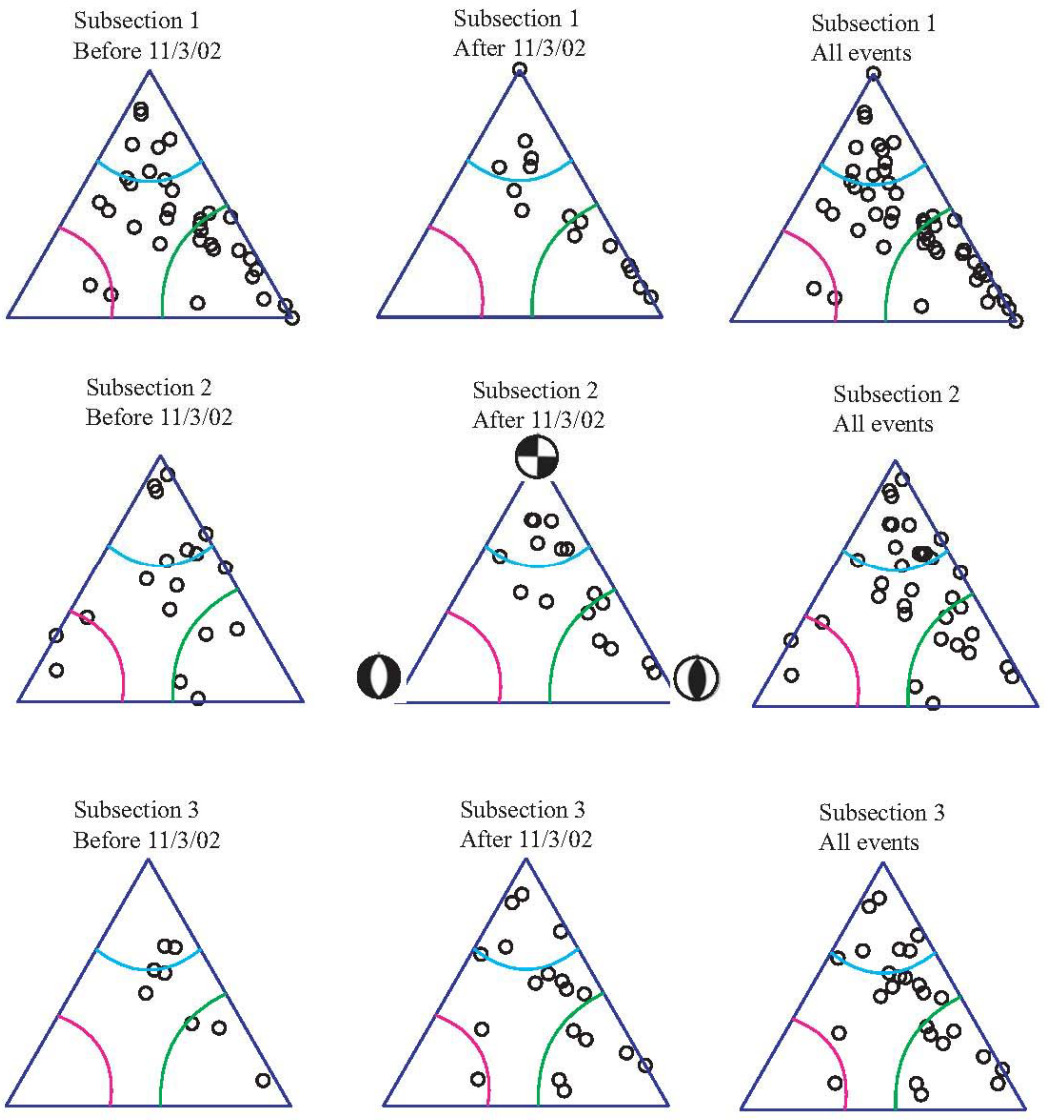

Figure 5.11 Triangle Diagrams from Each Subsection Before and After 2002.8. The first column shows the triangle diagram for each subsection before 2002.8. The second column shows the triangle diagram for each subsection after 2002.8 and the third column shows the triangle diagram for all events in each subsection. The colored bands represent the defining boundaries for standard strike-slip, reverse, and normal mechanisms. There are considerably fewer events in subsection 1 after 2002.8 making a comparison difficult. The trend appears to remain the same. Subsection 2 shows that there are fewer normal faulting events after 2002.8, but in general the trend remains roughly similar. In subsection 3, there are more events after 2002.8 making a comparison difficult. There are more normal events after 2002.8, but the trend in strike-slip and reverse events remains similar.

The stresses in the Kantishna Cluster change rapidly throughout the cluster. There is a counter-clockwise rotation of the maximum compression axis (P-axis) moving southward through the cluster. The types of mechanisms within the cluster are somewhat distributed with the vast majority falling in combinations between pure thrust and pure strike-slip. The stress tensor inversions comparing before and after the M_w7.9 event show that the stresses in the individual subsections may have changed as a result of the event. Subsections 1 and 2 show a transition from mostly strike-slip events to obliquely slipping events with a strong thrust component. However, the triangle diagrams for the two subsections show that the types of events are fairly similar before and after. The variance (or spread) of the events is the same for both stress tensor inversions (before and after), implying that although the best fitting stress tensor inversion results for before and after are different, the distribution of events is similar. Subsection 3 shows no change in the stress tensor inversion results, however, the small number of events before compared to after makes a comparison of the triangle diagrams difficult.

5.4 Coulomb Stress Change Calculations

The hypocentral relocations in chapter 3 allow fault planes to be inferred for the smaller sub-regions. The slip distribution of the M_w 7.9 Denali Fault event (Elliot et al., 2007) was put into the program Coulomb 3.0. The slip distribution of an input fault is used to calculate the predicted Coulomb stress change for an earthquake type on any number of receiver faults. The tendency of rocks to fail in a brittle manner is a function of both shear and confining stresses, or the Coulomb criterion. Coulomb stress changes

depend on the geometry and slip of an earthquake, the geometry and sense of slip on the receiver fault, and the effective coefficient of friction (Stein et al., 1994). Keeping this in mind, the inferred fault planes calculated in section 5.2 were input as receiver faults and the Coulomb stress change for right-lateral slip, left-lateral slip and reverse slip were calculated for coefficients of friction ranging from 0.1 to 0.7.

The results showed little difference, if any, for different values of the coefficient of friction. A common estimate for the coefficient of friction is 0.4 (Toda et al., 2005). The results for a coefficient of friction of 0.4 are shown in Figure 5.12. The top figure shows the location of the Kantishna Cluster with respect to the M_w 7.9 Denali Fault earthquake rupture. The axes are labeled as distance in kilometers from an origin; in this case 62°N-146°W. The Coulomb stress change on each portion of the Kantishna Cluster for each earthquake type is shown in the bottom three figures labeled left-lateral slip, right-lateral slip and reverse slip. An increase in Coulomb stress suggests that the fault would be brought closer to failure and a decrease in stress suggests failure would be retarded as a result of the precursory event (Lin and Stein, 2004).

Overall, the predicted Coulomb stress change values were generally small, ranging from -0.1 to 0.05 bars. The predicted Coulomb stress changes for sub-region A shows a decrease in left-lateral slip (-0.1 bar) and an increase in right-lateral (0.05 bar) and reverse slip (0.01 bar). The Coulomb stress changes predict an increase in right-lateral and reverse slip events. The predicted Coulomb stress change for sub-region B

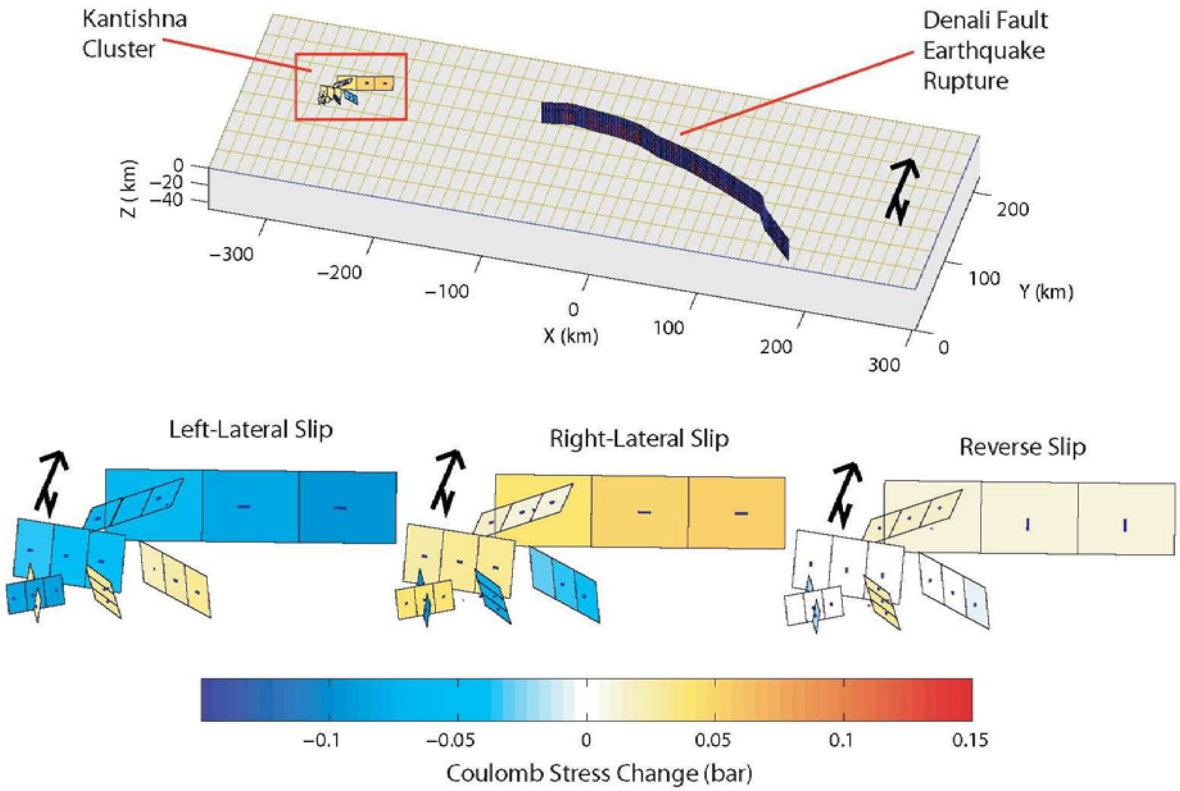

Figure 5.12 Coulomb Stress Change Predictions for Each Inferred Fault Plane Solution. The red box shows the position of the Kantishna Cluster to the M_w 7.9 Denali Fault earthquake rupture. The axes are labeled in kilometers from an origin with depth shown on the z-axis. The origin used in the map is 62°N-146°W. Below the map is shown the predicted Coulomb stress change for each faulting type, left-lateral, right-lateral, and reverse with a coefficient of friction of 0.4. Each inferred fault plane is shown with the southern most sub-region, E, shown with both possible fault planes. The Coulomb stress predictions are small, ranging from -0.1 to 0.05 bar. Increases in Coulomb stress imply that the fault was brought closer to failure and decreases imply that the fault was brought further from failure.

shows a decrease in left-lateral slip (-0.1bar) and an increase in right-lateral (0.01 bar) and reverse slip (0.01 bar). The predicted stress changes, albeit small changes, may account for the change seen in the stress tensor inversion from before and after the M_w7.9 event for subsection 1 in section 5.2 (Figure 5.4).

The predicted Coulomb stress changes for sub-region C show a decrease in left-lateral slip (0.1 bar) and an increase in right-lateral slip (0.04 bar). The predicted Coulomb stress changes for sub-region D show an increase in left-lateral slip (0.03 bar) and a decrease in right-lateral slip (-0.5 bar). Both sub-regions C and D show no predicted Coulomb stress change for reverse slip. The stress tensor inversion comparison for subsection 2 shows a change to more of an obliquely thrusting regime after the M_w 7.9 event; this is not seen in the predicted stress changes (Figure 5.12).

The predicted Coulomb stress changes for sub-region E shows an increase in left-lateral slip (0.04 bar) and reverse slip (0.03 bar), and a decrease in right-lateral slip (0.05 bar). Sub-region F shows a predicted increase in left-lateral slip (0.03 bar) and a predicted decrease in right-lateral (0.1 bar) and reverse slip (0.03 bar) for plane 1 (see Table 5.2). Sub-region F shows a predicted stress decrease for left-lateral slip (0.1 bar) and a stress increase for right-slip (0.4 bar) for plane 2 (Table 5.2). The stress tensor inversion comparison for before and after the M_w 7.9 event for subsection 3 showed no change in mechanism type.

The predicted Coulomb stress changes for the Kantishna Cluster are small, on the order of -0.1 to 0.05 bars. These small values are most likely related to the 150km distance between the cluster and the earthquake rupture. The predicted stress changes for

the two sub-regions of subsection 1 show good agreement with the results of the stress tensor inversions. The stress tensor inversions show a change to more of an obliquely thrusting regime, which match the predictions from the Coulomb stress calculations of increases in thrust and right-lateral motion. The predicted Coulomb stress changes for the two sub-regions in subsection 2 do not appear to match well with the stress tensor inversion results. The inversion results show a change to a more obliquely thrusting regime. The predicted Coulomb stress changes predict no increase in reverse slip. The predicted Coulomb stress changes for the two sub-regions in subsection 3 match to a certain degree. The Coulomb predictions show an increase in strike-slip behavior which is seen in the stress tensor inversions, however, the Coulomb stress predictions show an increase in reverse slip in sub-region E that is not seen in the stress tensor inversion results for subsection 3.

Chapter 6. Discussion of Results and Interpretations.

The Kantishna Cluster is a highly active and complicated region. Double difference hypocentral relocations show that the cloud of earthquakes in the cluster collapses down to six or more separate sub-regions. Cross sections show the seismicity in the cluster is generally confined to depths of 5-15km. The rate calculations for the Kantishna Cluster show that the rate is highly variable through time, ranging anywhere from 1 to 22 events ($M_L \geq 2$) per month. The stresses in the region are varied. Fault plane solutions for earthquakes with $M_L \geq 3$ show that mechanism types vary from pure strike-slip to pure thrust/reverse and everything in between. There are also a handful of normal faulting mechanisms in each subsection. The maximum compressive stresses show a counter-clockwise rotation from north to south through the cluster. From seismicity trends resolved from the double difference hypocentral relocations, a series of fault planes are inferred to define the region. The inferred faults are in agreement with the stresses described by the stress tensor inversions. These inferred fault planes show several different orientations which are reflective of the complicated stress environment surrounding the cluster.

Figure 6.1 shows the inferred fault planes in the Kantishna Cluster mapped with the tectonics surrounding the cluster. The yellow arrows represent the Bering block rotation (Cross and Freymueller, in press). The red arrows represent the rotation of southern Alaska (Eberhart-Phillips et al., 2003). The black arrows represent the average maximum compressive stress in the Kantishna Cluster, which is represented by its inferred faults.

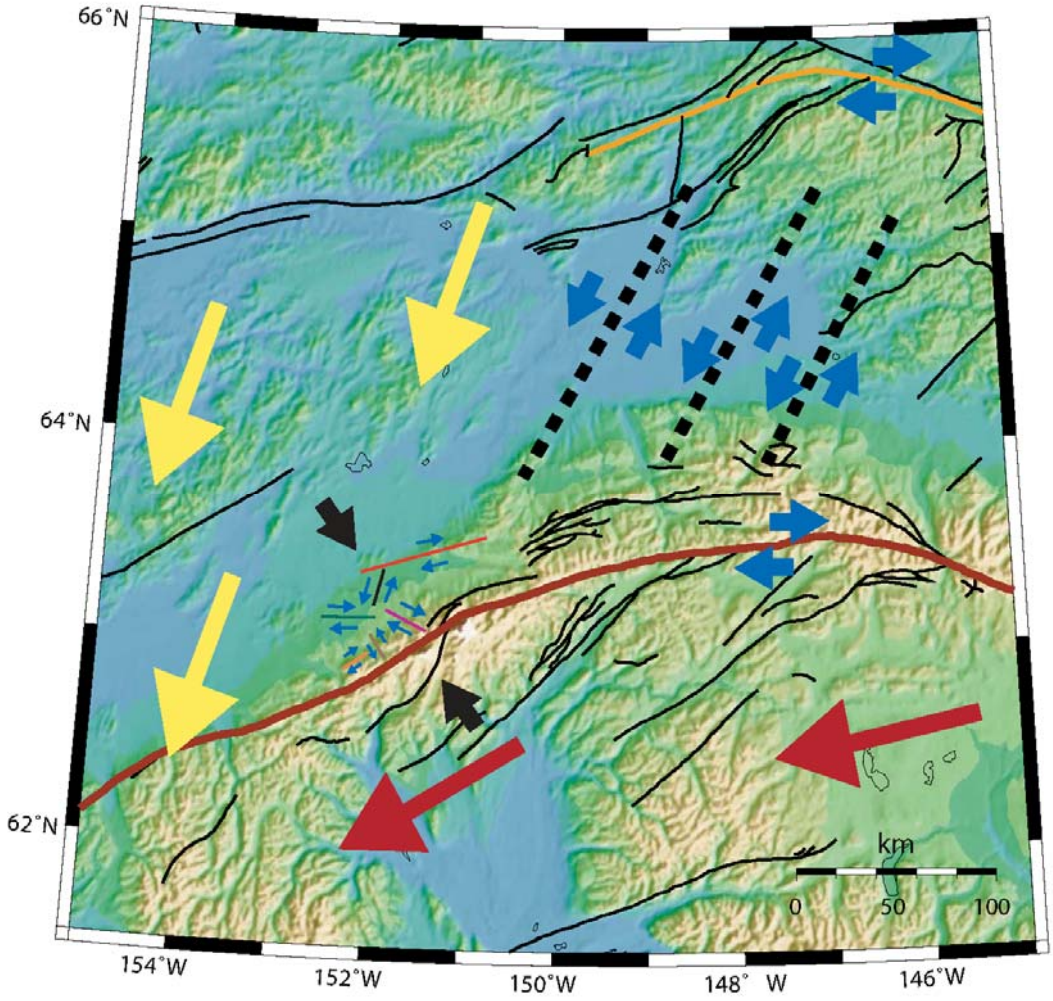

Figure 6.1 Map of the Big Picture. The above map shows the orientations of stresses in the proximity of the Kantishna Cluster with the inferred fault planes. The yellow arrows represent the Bering block rotation (Cross and Freymueller, in press). The red arrows represent the rotation of southern Alaska (Eberhat-Phillips et al., 2003). The black arrows represent the average maximum compressive stress in the Kantishna Cluster. The blue arrows represent strike-slip motion on the Denali Fault (dark red), Tintina Fault (orange), and the Minto Flats, Salcha, and Fairbanks seismic zones (black) (Page et al., 1991). The Kantishna Cluster is represented by the inferred faults with the motion on each fault shown with blue arrows.

The blue arrows represent strike-slip motion on the Denali Fault (dark red), Tintina Fault (orange), and the Minto Flats, Salcha, and Fairbanks seismic zones (black dashed lines). Looking at the inferred faults and the sense of motion on each, a fault model of the Kantishna Cluster can be proposed.

One possible explanation for the behavior in the Kantishna Cluster results from NNW-SSE compression due to Pacific plate convergence (Ratchkovski and Hansen, 2002; Eberhart-Phillips et al., 2003) and the presence of the bend in the Denali Fault. The faults labeled A through F in Figure 6.2 are the faults inferred from seismicity trends; with the maximum compressive stress directions plotted in black. The compression due to plate convergence (blue arrows) in the region causes two wedges to form separated by fault D (see Figure 6.2). The two wedges, named East Wedge and West Wedge, accommodate the shortening of the region compensated for on faults B and D.

Faults A, B, D and the Denali Fault bound the East Wedge. The thrust on Fault A is due to the compression of the East Wedge and the slight eastward motion from the East Wedge being "squeezed out" to the east. Seismicity along the portion of the Denali fault bounding the East wedge is minimal and may be either partially locked or aseismically slipping. The thrust on fault A potentially compensates for the lack of motion on the Denali fault. Lesh and Ridgeway (2007) showed that the northern portion of the Kantishna Cluster (sub-region A) is actively uplifting. This uplift is in agreement with an actively thrusting environment. The West Wedge is bounded by faults C, D, and the Denali Fault. This wedge is being "squeezed" to the west compensating for compression. The rotation of the Bering Block and the rotation of southern Alaska potentially pinch off

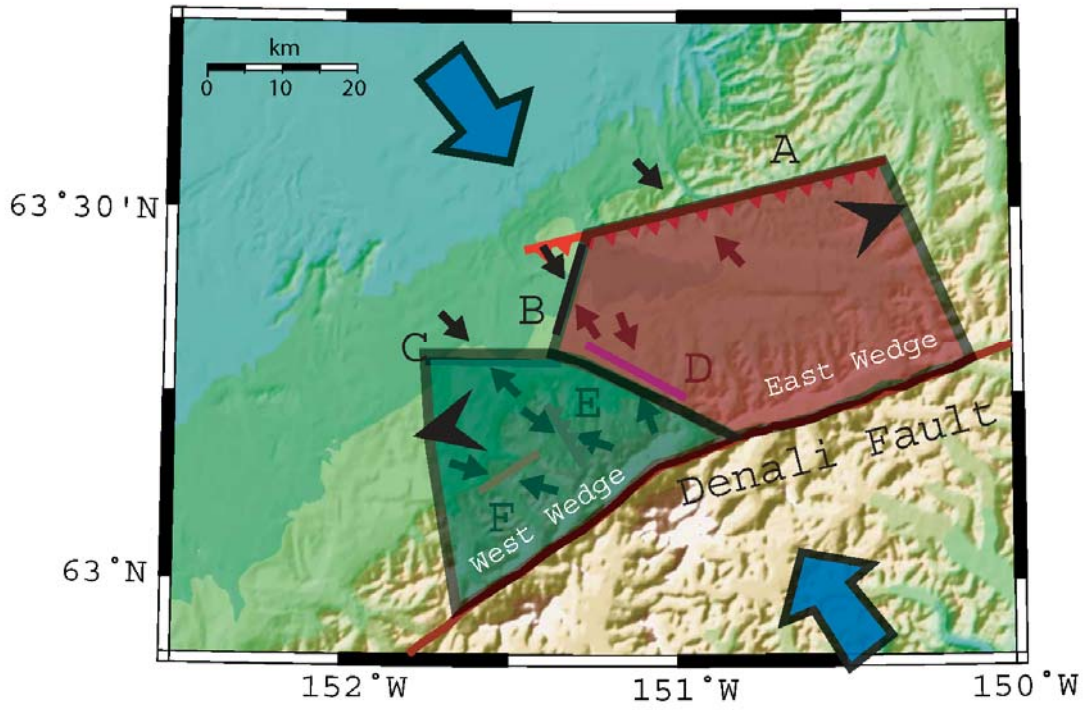

Figure 6.2 Wedges Plot. The two wedges proposed to represent the motions in the Kantishna Cluster are plotted above with the inferred fault planes uncovered from seismicity trends. The Small black arrows represent the maximum compressive stresses on each of the inferred fault planes. The larger black arrows represent the sense of motion of the wedges. The large blue arrows represent the regional stress due in large part to the subduction of the Pacific plate (Ratchkovski and Hansen, 2002; Eberhart –Phillips, 2003). The compression due to plate convergence causes shortening across the Kantishna Cluster via faults B and D. The wedges labeled East Wedge and West Wedge, are being "squeezed out" as a result of the compression and motion of the wedges is accommodated on the inferred faults. Faults E and F accommodate internal deformation of the West Wedge.

motion on this portion of the Denali Fault and allow a westerly motion of the West Wedge. Faults E and F then represent internal deformation of the West Wedge. The increase in seismicity seen in sub-regions E and F is likely related to changes in stress resulting from the M_w7.9 Denali Fault earthquake. The model proposed requires further testing and verification, by use of combined seismic, geodetic and geologic data.

Looking at the cluster with respect to the M_w 7.9 Denali Fault earthquake shows that the earthquake appears to have had little effect on the cluster. The seismicity rate per month shows that the rate was highest in the mid-1990s. When the rate, for the whole cluster, from 1999-2002.8 was compared to after the earthquake (2002.8-2006.25), there were only small changes in seismicity. Breaking the seismicity into subsections shows more subtle changes. In subsection 1 (the northernmost section) the rate decreased by 0.2 events per month on average. Subsection 2 (the central section) showed an increase of 0.5 events per month on average. Subsection 3 (the southernmost section) showed an increase of 1.4 events per month on average, doubling the previous average. The z-value shows that there was a small increase in seismicity (decrease in z-value) in late 2002-early 2003. The z-value, which is relative to the long term average, decreased from 2.5 to 1 and continued decreasing until 2004. This increase is likely related to the increase in seismicity of subsection 3. Spatially through the cluster, there were small patches of increased and decreased z-values. The b-values show that there were small patches of increased and decreased b-values, but overall the b-value didn't change. These small changes occur in both time period comparisons. Small changes in z- and b-values as well as rate (number per month) are difficult to interpret due to the high and variable

background seismicity rate. This high background tends to mask changes occurring later in time. The small increases seen in the z- and b-value maps can be related to the M_w7.9 Denali Fault earthquake because they are resolved independently using the higher and lower background rates, which are compensated for by using the two different time intervals (1990-2002.8 and 1999-2002.8).

The stress tensor inversion comparisons before and after the M_w 7.9 event show that subsections 1 and 2 experienced a change from predominately strike-slip to a more obliquely thrusting regime, and subsection 3 remained the same. The distribution of mechanism type, plotted as ternary diagrams, shows that overall the mechanism types in each subsection are similar. The only real change observed is the number of events and the number of normal faulting events. The distribution of events shows that the changes observed in the stress tensor inversions are most likely related to the number of events used in each inversion. The lack of normal faulting events after the M_w 7.9 event in subsections 1 and 2 cannot be overlooked. It is likely that the lack of normal faulting events is related to postseismic changes associated with the M_w 7.9 event; however, these changes are not necessarily indicative of a causative relationship between the Denali fault and the Kantishna Cluster. The stress tensor inversion results for subsection 3 show no change in the best fitting stress tensor, despite the occurrence of normal faulting events. The Coulomb stress change predictions are small, on the order of -0.1 to 0.05 bars. The small values are related to the large distance (150km) between the cluster and the earthquake rupture. However, several of the Coulomb stress change predictions agree well with the stress tensor inversions, such as an increase in thrusting environment for

subsections 1 and 2, but the changes are not well represented in the ternary/triangle diagrams. The Coulomb stress change predictions are predictions of event type based on the geometry of the receiver fault and the Coulomb criteria; however, the types of events predicted may be far enough from failure that they may not be observed (Stein et al., 1994).

The small changes seen in the northern and central Kantishna Cluster after the M_w 7.9 Denali Fault earthquake appear to coincide in the time with the earthquake, and do not appear to show a strong causative relationship between the cluster and the Denali Fault. Small pockets of change are not indicative of an overall influence of the Denali Fault system on the Kantishna Cluster. The lack of a clear pattern in the seismicity and stresses in the northern and central Kantishna Cluster make comparisons difficult. There are noticeable changes that coincide with the M_w 7.9 event. These changes, albeit small, can not be ignored; however, a direct causative relationship to the Denali Fault can not be decidedly determined.

Subsection 3, on the other hand, showed a dramatic increase in seismicity and b-value that can be directly related to the M_w 7.9 event. The proximity and obvious seismicity influence of the Denali Fault imply a strong causative relationship between the Denali Fault and subsection 3 of the Kantishna Cluster.

Further research related to the Kantishna Cluster should involve doing moment tensor inversions to calculate additional fault plane solutions. More fault plane solutions with a better spatial distribution throughout the cluster would allow a stress map to be calculated. From a stress map, subtle changes progressing through the cluster would be

uncovered. In addition to refining the inferred fault planes, a more thorough time step look at the stress changes with time would be possible. Cross-correlation of waveforms used in hypocentral relocations and the inclusion of data from a temporary, tighter, broadband network would help to better constrain the inferred fault planes. The combination of geodetic data with seismic data would also help to refine the model based on the inferred faults.

References:

Bundtzen, T.K. (1981). Geology and mineral deposits of the Kantishna Hills, Mount McKinley Quadrangle, Alaska, *M.S. Thesis*, University of Alaska Fairbanks, 238pp.

Cross, R., J.T. Freymueller (in press). Evidence for and Implications of a Bering Plate Based on Geodetic Measurements from the Aleutians and Western Alaska, submitted to *J. Geophys. Res.*.

Eberhart-Phillips, D., P.J. Haeussler, J.T. Freymueller A.D. Frankel, C.M. Rubin, G.A. Carver, A.J. Crone, T.E. Dawson, H. Fletcher, R. Hansen, E.L. Harp, R.A. Harris, D.P. Hill, S. Hreinsdottir, R.W. Jibson, C.F. Larsen, S.C. Moran, S.F. Personius, G. Plafker, B Sherrod, K. Seih, N. Sitar, W.K. Wallace (2003). The Denali Fault Earthquake, Alaska: A Large Magnitude, Slip-Partitioned Event, *Science*, **300**, 1113-1118.

Elliott, J.L., J.T. Freymueller, B. Rabus (2007). Coseismic Deformation of the 2002 Denali Fault Earthquake: Contributions from Synthetic Aperture Radar Range Offsets, *J. Geophys. Res.,* 112, B06421, doi: 10.1029/2006JB004428.

Eppinger, R.G., P.H. Briggs, J.G. Crock, A.L. Meier, S.J. Sutley, P.M. Theodorakos, (2000). Environmental-Geochemical Study of the Slate Creek Antimony Deposit, Kantishna Hills, Denali National Park and Preserve, Alaska, *U.S. Geological Survey Professional Paper,* 1662.

Frohlich, C. (1992). Triangle Diagrams: Ternary Graphs to Display Similarity and Diversity of Earthquake Focal Mechanisms, *Phys. of the Earth and Planetary Interiors*, **75**, 193-198

Gutenberg, B., C.F. Ricter (1944). Frequency of earthquakes in California, *Bull. Seis. Soc. Am.,* **34**, 185-188.

Lay, T., T.C. Wallace (1995). *Modern Global Seismology*, Academic, San Diego, Calif.,.

Lesh, M.E., K.D. Ridgeway (2007). Geomorphic Evidence of Active Transpressional Deformation in the Tanana Foreland Basin, South-Central Alaska, in Ridgeway, K.D., Trop, J.M., Glen, J.M.G., and O'Neill, J.M., eds., Tectonic Growth of a Collisional Continental Margin: Crustal Evolution of Southern Alaska, Geological Society of America Special Paper 431, 573-592, doi: 10.1130/2007.2431(22).

Lin, J., R.S. Stein (2004). Stress Triggering in Thrust and Subduction Earthquakes and Stress Interaction Between the Southern San Andreas and Nearby Thrust and Strike-Slip Faults, *J. Geophys. Res*. **109**, B02303, doi:1029/2003JB002607.

McNutt, S.R. (2002). Volcano Seismology and Monitoring for Eruptions, *Int. Handbook Earthquake and Engineering Seismology*, **81A**, 383-406.

Meyers, E.V., D.H. Christensen, G.A. Abers, J.C. Stachnik, A.R. Holland, K.B. Beebe (2000). Broadband (seismic) Experiment Across the Alaska Range (BEAAR) to Determine the Crustal and Upper Mantle Structure Beneath Central Alaska, *EOS* **81**, F877.

Michael, A.J. (1984). Determination of Stress From Slip Data: Faults and folds, *J. Geophys. Res.* **89**, 11517-11526.

Michael, A.J. (1987). Use of Focal Mechanisms to Determine Stress: A Control Study, *J. Geophys. Res.* **92**, 357-368.

Page, R.A., N.N. Biswas, J. C. Lahr, H. Pulpan (1991). Seismicity of continental Alaska, in Neotectonics of North America. D.B. Slemmons, E.R. Engdahl, M.D. Zpback, and D.D. Blackwell (Editors), Geological Society of America, Boulder, CO, Decade Map Volume 1, 47-68.

Page, R. A., G. Plafker, H. Pulpan (1995). Block Rotation in East-Central Alaska: A Framework for Evaluating Earthquake Potential? *Geology* **23**, 629-632.

Paige, C.C., M.A. Saunders (1982). LSQR: An Algorithm for Sparse Linear Equations and Sparse Least Squares, *ACM Trans. Math. Softw.* **8**, 43-71.

Ratchkovski, N.A. (2001). Seismological Constraints on Tectonics of Southern and Central Alaska: Earthquakes Locations and Source Mechanisms, *PhD. Thesis*, University of Alaska, Fairbanks, 149pp.

Ratchkovski, N.A., R.A. Hansen (2002). New Constraints on Tectonics of Interior Alaska: Earthquake locations, Source Mechanisms, and Stress Regime, *Bull. Seis. Soc. Am.* **92**, 998-1014.

Reasenberg, P. (1985). Second Order Moment of Central California Seismicity, 1969-1982, *J. Geophys. Res.* **90**, 5479-5495.

Reasenberg, P.A., D. Oppenheimer (1985). FPFIT, FPPLOT and FPPAGE: Fortran Computer Programs for Calculating and Displaying Earthquake Fault-Plane Solutions, *U.S. Geol. Surv. Open-File Rept. 85-739*, 109pp.

Stein, R.S. C.P. King, J. Lin (1994). Stress Triggering of the 1994 M=6.7 Northridge, California, Earthquake by its Predecessors, *Science,* **265**, 1432-1435.

Talwani, P. (1999). Fault Geometry and Earthquakes in Continental Interiors, *Tectonophysics*. **305**, 371-379.

Toda, S., R.S. Stein, K. Richards-Dinger, S.B. Bozkurt (2005). Forcasting the Evolution of Seismicity in Southern California: Animations Built on Earthquake Stress Transfer, *J. Geophys. Res.* **110**, B05S16, doi:10.1029/2004JB003415, 17pp.

Veenstra, E., D.H. Christensen, G.A. Abers, A. Ferris (2006). Crustal Thickness Variation In South-Central Alaska, *Geology*. **34**, 781-784.

Waldhauser, F. (2001). HypoDD-A Program to Compute Double-Difference Hypocentral Locations, *U.S. Geol. Surv. Open-File Rept. 01-113*, 25pp.

Waldhauser, F., W. Ellsworth (2000). A Double Difference Earthquake Location Algorithm: Method and Application to the Northern Hayward Fault, California, *Bull. Seis. Soc. Am*. **90**, 1353-1368.

Weimer, S. (2001). A Software Package to Analyze Seismicity: ZMAP, *Seis. Res. Letters.,* 72 (2), 373-382.

Wyss, M., S. Weimer, R. Zuniga (2001). ZMAP: A Tool for Analyses of Seismicity Patterns. Typical Applications and Uses: A Cookbook, 64pp.